Journal of Materials Chemistry B

ROYAL SOCIETY OF CHEMISTRY

PAPER

View Article Online
View Journal | View Issue

Cite this: J. Mater. Chem. B, 2025, 13, 12205

Sodium alginate/polyvinylpyrrolidone/lapatinib-loaded Zr–metal organic framework: biocompatibility evaluation and pH-responsive *in vitro* drug release for oral delivery applications

Sneha Rajeev, Naja Hasoon K T and Unnikrishnan Gopalakrishna Panicker *

Recent advancements in drug delivery systems have transformed drug administration methods to ensure precise, targeted delivery with minimal side effects. Innovations involving polymer–metal organic frameworks can significantly improve drug stability and controlled release properties. In this study, a drug delivery system based on a zirconium metal organic framework (Zr-MOF), sodium alginate (SA), and polyvinylpyrrolidone (PVP) was developed. Lapatinib, an oral anticancer drug used to treat breast cancer, was incorporated into the pores of a Zr–metal organic framework. Although lapatinib selectively inhibits HER2 receptors and cancer cell proliferation, it has limitations, primarily due to its poor oral bioavailability and side effects resulting from its toxicity. To address these issues, we embedded a drug-loaded Zr–metal organic framework in a sodium alginate (SA)/polyvinylpyrrolidone (PVP) polymer matrix. This combination has been proposed to modulate drug release characteristics, promote pH-responsive targeted drug delivery, increase stability, enhance mechanical properties (tensile strength of 6.5 MPa), improve hydrophilicity, and potentially enhance biocompatibility of the composites. *In vitro* release studies showed minimal lapatinib release (13%) over 48 h under simulated gastric conditions (pH 1.2), whereas drug release reached 91% at intestinal pH (6.8) during the same period. These findings indicate that the system can intrinsically prevent premature gastric release, emphasizing its potential to achieve high therapeutic effects at lower doses with reduced side effects. Biocompatibility assays indicated over 94% viability in the relevant cell lines after 24 and 48 h, indicating the favorable cytocompatibility of the composites. Overall, this composite platform provides controlled, sustained, and site-specific release of lapatinib, which could potentially enhance oral bioavailability, reduce dosage frequency, and systemic toxicity.

Received 17th June 2025,
Accepted 21st August 2025

DOI: 10.1039/d5tb01449b

rsc.li/materials-b

1. Introduction

Cancer remains one of the leading causes of death worldwide, and the development of novel and efficient cancer therapy approaches is viewed as an essential and critical step in cancer treatment protocols. Cancer-drug delivery technology presents a fascinating interdisciplinary challenge in various fields, including pharmaceuticals, chemical engineering, biomaterials, and medical communication. This technology represents a cutting-edge area of science that requires a multidisciplinary approach, ultimately contributing to the improvement of human healthcare.[1–3] Advancements in pharmaceutical technology have paved the way for the development of innovative methods of drug administration and the design and implementation of controlled-release formulations that precisely target site-specific actions.[4,5]

Conventional cancer therapy methods often have critical problems associated with them, such as low selectivity, poor bioavailability, and systemic toxicity, which can harm healthy and cancerous cells. To overcome these obstacles, controlled release and pH-responsive drug delivery systems have gained attention as promising approaches for improving therapeutic efficacy while minimizing adverse effects.[6,7] By integrating stimuli-responsive mechanisms, these systems can provide targeted release triggered by environmental factors such as pH changes in different biological compartments.[8,9]

Lapatinib, also known as TykerbTM, is a dual-kinase inhibitor used in the management of breast cancer and various other solid tumors. This oral medication belongs to a class of targeted cancer therapies called "tyrosine kinase inhibitors".[10,11] Lapatinib dissolves in the digestive system upon ingestion and is subsequently absorbed into the bloodstream. Its primary function is to target cancer cells that specifically express HER2 receptors. Thus, lapatinib effectively hinders the division of cancer cells, impeding the formation of new

Department of Chemistry, National Institute of Technology Calicut, 673601, Kerala, India. E-mail: sneha_p220269cy@nitc.ac.in, unnig@nitc.ac.in

malignant cells.[12] Despite its efficacy against HER2 breast cancer, the clinical utility of lapatinib is limited by its poor solubility (<0.0001 mg mL), off-target toxicity (25% discontinuation rate), and rapid metabolism. Conventional formulations fail to address these issues, as evidenced by their low tumor accumulation (5%) and high dosing frequency (1500 mg per day).[13,14]

Zr–metal organic frameworks (Zr-MOFs) are hybrid organic–inorganic materials composed of ordered networks of zirconium and organic linkers. These materials have garnered significant attention in recent years owing to their remarkable characteristics, including their high surface area, porosity, and ability to tune their chemical and physical properties.[15,16] The distinctive structure of Zr–metal organic frameworks allows for precise control over pore size and functionality, making them highly promising drug delivery vehicles. Zr-MOFs enable efficient drug loading and controlled release owing to their well-defined pore structures. Despite these advantages, pure MOFs face challenges, including rapid drug release and potential cytotoxicity, which limit their *in vivo* applicability.[17–19]

To mitigate these limitations, encapsulating MOFs with biocompatible polymer matrices, such as sodium alginate (SA) and polyvinylpyrrolidone (PVP), can be a promising strategy. This can modulate drug release kinetics, enhance mechanical stability and flexibility, improve biodegradability, and reduce toxicity.[20,21] Nevertheless, research integrating Zr-MOFs with SA/PVP composites, specifically for delivering hydrophobic anticancer agents such as lapatinib, remains limited.

Recent advances have emphasized the necessity of oral chemotherapy platforms that provide sustained, pH-responsive, and biocompatible drug delivery systems to enhance patient compliance and improve therapeutic outcomes. Recent efforts have focused on nanocarriers, such as polymeric nanoparticles,[22] lipid-based systems,[23] and MOF-based formulations,[24] to improve the bioavailability of lapatinib and reduce its systemic toxicity. However, most systems either lack sufficient protection in gastric environments, leading to premature drug release and low oral bioavailability,[25] or exhibit burst-release profiles that undermine sustained therapeutic action.[26] Furthermore, concerns regarding the cytotoxicity and scalability persist for uncoated MOFs and non-biopolymer matrices.[27,28]

Despite some advances, there remains a clear need for a delivery platform that combines (i) protection against degradation, (ii) pH-responsiveness and controlled release in intestinal and tumoral environments, (iii) enhanced biocompatibility, and (iv) robust mechanical properties suitable for oral administration. To date, the integration of Zr-MOFs within biocompatible, hydrophilic polymer films, such as sodium alginate (SA) and polyvinylpyrrolidone (PVP), which may collectively address these shortcomings, has scarcely been explored for lapatinib or other similar hydrophobic drugs. Therefore, this study aimed to develop and characterize a novel SA/PVP/Zr-MOF composite film for lapatinib delivery and assess its physicochemical properties, biocompatibility, and pH-responsive drug release, thereby providing a potential solution to the unresolved challenges of effective oral and targeted cancer chemotherapy. It offers the potential to reduce dosing frequency and systemic side effects, which could ensure better patient compliance and therapeutic outcomes.

2. Materials and methods

2.1. Materials

Zirconium tetrachloride ($ZrCl_4$, Sigma Aldrich, 99.5%), terephthalic acid (Sigma Aldrich, 98%), *N*,*N*-dimethylformamide (DMF, Sigma Aldrich, 99.8%), formic acid (HCOOH, Sigma Aldrich), anhydrous chloroform (CHCl3, Sigma Aldrich, 99%), polyvinylpyrrolidone (PVP, Spectrochem), sodium alginate (SA, Kanton chemicals) and lapatinib (Lap, Hetero healthcare limited) are the materials involved in this work.

2.2. Synthesis of Zr-MOF (UiO-66)

In a 250 mL flat-bottom flask, 0.75 g (4.5 mmol) of terephthalic acid, 1.05 g (4.5 mmol) of zirconium tetrachloride, and 40 mL of *N*,*N*-dimethylformamide (DMF) were initially ultrasonicated for 1 h. Formic acid (17 mL, 450 mmol) was added as a modulator to the mixture. The flask was sealed with Teflon tape and heated in an oven at 120 °C for 24 h. Filtration was subsequently performed, and the product was ultrasonically washed with 15–20 mL of anhydrous chloroform for 30 min. The product was collected and vacuum-dried at room temperature for 24 h. A schematic representation of the synthesis of Zr-MOFs is presented in Fig. 1.[29]

2.3. Preparation of lapatinib-loaded Zr-MOF

The Zr-MOF was subsequently loaded with different weight percentages of lapatinib [20, 30, 40, and 50%]. Typically, lapatinib (0.125, 0.215, 0.335, and 0.5 g) was dissolved in 20 mL DMF, and Zr-MOF (0.5 g) was added. It was stirred for 24 hours and then centrifuged at 3000 revolutions per minute (RPM), filtered, and dried at room temperature for 24 h. The prepared lapatinib-loaded Zr-MOF samples were labelled as LZ20, LZ30, LZ40, and LZ50 for 20, 30, 40, and 50 weight

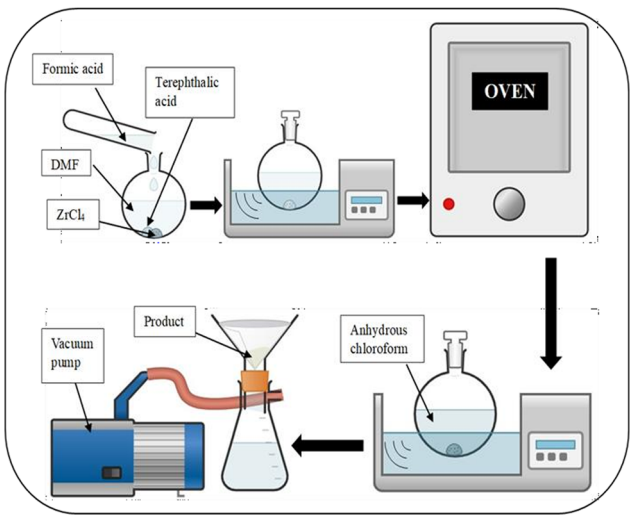

Fig. 1 Synthesis of Zr–metal organic framework (UiO-66).

Table 1 Sample codes for different weight percentages of lapatinib-loaded Zr–metal organic frameworks (LZ20, LZ30, LZ40, and LZ50 for 20, 30, 40, and 50 weight percent (wt%) of lapatinib, respectively)

Sample code	Lapatinib amount (g)	Zr-MOF amount (g)	Lapatinib wt%
LZ20	0.125	0.500	20%
LZ30	0.215	0.500	30%
LZ40	0.335	0.500	40%
LZ50	0.500	0.500	50%

percent (wt%) of lapatinib, respectively. The sample codes are listed in Table 1.

2.4. Preparation of sodium alginate/polyvinylpyrrolidone films

Different weight percentages of sodium alginate (90, 80, and 70%) and polyvinylpyrrolidone (10, 20, and 30%) were dissolved in distilled water using a magnetic stirrer for 4–5 h. The mixture had a total mass of 2.5 g. The mixture was then poured into glass molds and kept at room temperature for 24 h, followed by drying in a hot air oven at 60 °C for 4 h to complete the drying. The prepared samples possessed weight percentages of 90%, 80%, and 70% SA and 10%, 20%, and 30% PVP, respectively.[30] The samples were labeled SP1, SP2, and SP3 (Table 2).

2.5. Preparation of sodium alginate/polyvinylpyrrolidone/lap-loaded Zr-MOF films

In a typical procedure, the optimized weight% of the SA/PVP blend (90 : 10) was dissolved in distilled water and stirred with a magnetic stirrer for 4–5 hours. Specific weight percentages (5, 10, 15, and 20%) of lapatinib-loaded Zr-MOF were added. The mixture was stirred for 3 h and poured into a glass mold. Composite films were obtained after complete drying at room temperature for 24 h and at 60 °C for 4 h. The procedure was repeated for different weight percentages of lapatinib-loaded Zr-MOF. The samples contained 0.132, 0.278, 0.441, and 0.625 g of lapatinib-loaded Zr-MOF and 2.5 g of the optimized SA/PVP blend (90 : 10 SA/PVP). The samples were labeled as SPLZ5, SPLZ10, SPLZ15, and SPLZ20, and the sample codes are detailed in Table 3. Fig. 2 shows the preparation of sodium alginate/polyvinylpyrrolidone/lapatinib-loaded Zr–metal organic framework composite films.

2.6. Characterization

2.6.1. Fourier transform infrared (FTIR) analysis. The Zr-MOF, lapatinib-loaded Zr-MOF, polymer blends of different ratios, and the drug-loaded polymer-MOF composite systems were examined by FTIR spectroscopy using a spectrometer (JASCO FTIR-4700) in the range of 4000 to 500 cm^{-1}. The samples were scanned in attenuated total reflectance (ATR) mode.

Table 2 Sample codes for sodium alginate/polyvinylpyrrolidone films (weight percentages of 90%, 80%, and 70% SA and 10%, 20%, and 30% PVP, labelled as SP1, SP2, and SP3)

Sample code	SA : PVP ratio
SP1	90 : 10
SP2	80 : 20
SP3	70 : 30

Table 3 Sample codes for sodium alginate/polyvinylpyrrolidone/lap-loaded Zr-MOF films (5, 10, 15, and 20% of lapatinib-loaded Zr-MOF with the optimized SA/PVP blend (90 : 10 SA/PVP), labelled as SPLZ5, SPLZ10, SPLZ15, and SPLZ20, respectively)

Sample code	Lapatinib-loaded Zr-MOF wt%	SA : PVP ratio
SPLZ5	5%	90 : 10
SPLZ10	10%	90 : 10
SPLZ15	15%	90 : 10
SPLZ20	20%	90 : 10

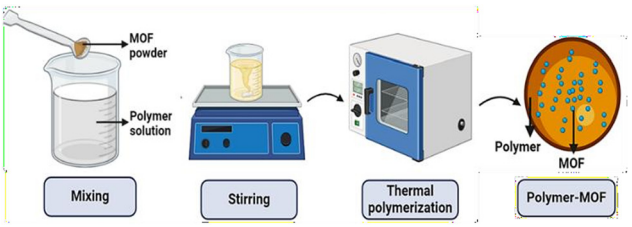

Fig. 2 Preparation of sodium alginate/polyvinylpyrrolidone/lapatinib-loaded Zr–metal organic framework composite films.

2.6.2. X-ray diffraction (XRD) analysis. The Zr-MOF, drug-loaded Zr-MOF, optimized SA/PVP film, and SA/PVP/Lapatinib-loaded Zr-MOF were subjected to crystallinity examination using a Miniflex-600-Rigaku benchtop X-ray diffractometer. The source was Cu-Kα with a scanning range of 5–90°. The measurements were performed at an operating voltage of 40 kV and a scan rate of 5° min^{-1}.

2.6.3. Thermogravimetric analysis (TGA). The thermal stabilities of the Zr-MOF, drug-loaded Zr-MOFs, blend systems, and composite systems were monitored using a thermogravimetric analyzer (TGA Q50). The experiments were performed in the temperature range of 25–700 °C at a heating rate of 10° min^{-1} under a nitrogen atmosphere.

2.6.4. Mechanical properties. The mechanical properties of the polymer blends and composites were examined using a Universal Testing Machine (UTM) (Shimadzu, Japan). The thicknesses of the films were measured using a digital screw gauge (Mitutoyo digital liquid crystal display (LCD) Micrometer Screw Gauge). The samples were cut into dumbbell-shaped films using 40 × 6 × 2 mm^3 molds. Sample preparation and testing were performed according to the American Society for Testing and Materials (ASTM) standard D412 (2002), at room temperature. Three samples of each membrane were used to determine the mechanical properties, and the average values were reported. The Young's modulus, ultimate tensile strength (UTS), and elongation at break were evaluated. The mechanical tests included pure SA/PVP polymer films as controls. Statistical analysis of the mechanical properties was performed using one-way ANOVA; $p < 0.05$ was considered significant.

2.6.5. Surface wettability. Static water contact angles were measured at room temperature using a Digidrop goniometer (GBX instrument, France). For each test, a 2 μL droplet of

Millipore water was carefully deposited on the membrane surface using a microsyringe fitted with a 20-gauge needle. The contact angle formed at the liquid–solid interface was determined by analyzing the images captured using the built-in camera of the instrument. To ensure accuracy, measurements were performed at three distinct locations on each sample to reduce potential experimental errors.

2.6.6. Moisture uptake and swelling ratio. To measure moisture absorption, the membranes were cut into 10 mm × 10 mm squares and dried in a desiccator containing calcium chloride for 24 h to establish their initial dry weight (W_o). Subsequently, the samples were transferred to a desiccator containing a saturated sodium chloride solution to create a humid environment. The weight of each membrane was recorded at regular intervals until equilibrium was reached (W_c). The moisture uptake percentage was determined using the following equation based on the difference between W_o and W_c:[31]

$$\text{Moisture uptake (\%)} = (W_c - W_o)/W_o \quad (1)$$

The swelling ratio was determined using the following method. The membranes were completely dried in an oven at low temperatures. The initial dry weights (W_o) of the membranes were measured using an analytical balance. Phosphate-buffered saline (PBS, pH 6.8) was used as the swelling medium to mimic physiological conditions. The dry films were immersed in a swelling medium, allowing them to be completely submerged. The films were carefully removed from the medium at specific time intervals (10 min, 30 min, 1 h, 2 h, 4 h, 6 h, 12 h, and 24 h). The swollen films were weighed immediately after blotting, and the swollen weight (W_t) was recorded at each time point. Statistical analysis was performed using one-way ANOVA. The swelling ratio, which indicates the water uptake by the film, was calculated using the following equation:[32]

$$\text{Swelling ratio (\%)} = (W_t - W_o)/W_o \times 100 \quad (2)$$

2.6.7. Surface morphology analysis. The morphologies of the optimized blend, drug-loaded Zr-MOF, and SA/PVP/Lap-loaded Zr-MOF systems were examined using scanning electron microscopy (SEM) [Carl Zeiss EVO 18 Research] with an accelerating beam voltage of 2 kV at 50×, 100×, and 500× magnification for each sample.[33]

Transmission electron microscopy (TEM) was performed using a BioTwin instrument operated at 120 kV. For imaging, the samples were prepared by dispersing 1 mg of the sample in 1 mL of ethanol and sonicated for 5 min. A drop of the resulting suspension was deposited onto a copper grid coated with a porous carbon film and dried in air. Images were acquired in bright-field mode, and the crystalline structure was confirmed using selected-area electron diffraction (SAED). The particle size distributions were determined from at least 100 particles using ImageJ software.[34]

2.6.8. Brunauer–Emmett–Teller (BET) analysis. The specific surface areas of the samples were determined by nitrogen adsorption at 77 K using a Belsorp-Max surface area and porosity analyzer. Before the measurements, each sample (~100 mg) was degassed under vacuum at 150 °C for 12 h. Nitrogen adsorption–desorption isotherms were measured over a relative pressure (P/P_0) range of 0.05–0.3. The BET surface area was calculated by applying the Brunauer–Emmett–Teller equation to the adsorption data using the manufacturer's software.[35]

2.6.9. *In vitro* biocompatibility evaluation

2.6.9.1. Hemolytic assay. The hemocompatibility of the polymer composites was evaluated using hemolysis testing.[36] Fresh human blood was collected from a healthy donor in an ethylenediaminetetraacetic acid (EDTA)-coated polypropylene (PP) tube to prevent coagulation and diluted with 0.9% saline. Square-shaped test samples (1 × 1 cm^2) were placed in PP tubes with 10 mL saline and pre-incubated at 37 °C for 30 min. Subsequently, 0.2 mL of diluted blood was added to each tube, followed by incubation at 37 °C for 60 min. Saline-blood and distilled water-blood mixtures were used as negative and positive controls, respectively, to establish the baseline and maximum hemolysis. Post incubation (24 h), the supernatant was extracted, and the absorbance was measured at 541 nm using ultraviolet-visible (UV-vis) spectroscopy. Statistical analysis was performed using one-way ANOVA, and statistical significance was set at $p < 0.05$. The hemolysis percentage was determined by averaging the results of triplicate tests using the following equation:[37]

$$\text{Hemolysis (\%)} = [\text{OD (test)} - \text{OD (negative control)}]/[\text{OD (positive control)} - \text{OD (negative control)}] \times 100 \quad (3)$$

where OD represents optical density.

2.6.9.2. Cytotoxicity evaluation. Cytotoxicity was assessed using L929 cell cultures according to ISO10993-5. A 48-well plate was used to seed the cells, which were then incubated overnight. Once the cells reached confluence, sterile materials were added to the cell-seeded plates. The cytotoxicity of the polymer composite system was examined using a direct-contact assay. L929 mouse fibroblast cells (1 × 104 cells per mL) were seeded in a 24-well plate (Becton, Dickinson and Company (BD) Falcon) and allowed to proliferate for 24 h to form a subconfluent layer. The material (diameter: cm) was placed over the monolayer and allowed to proliferate in a CO_2 incubator. After 24 h of incubation, cell morphology was evaluated using a control (cells grown without materials) under an inverted phase-contrast microscope (Olympus CKX41) with an attached imaging camera. Phase-contrast microscopy was used to track morphological changes in the cells and quantify the percentage of surviving fibroblast cells using the 3-(4,5-dimethylthiazole-2-yl)-2,5-diphenyltetrazolium bromide (MTT) assay.[38]

The MTT assay was used to count the number of viable cells and assess the viability of mitochondrial cellular metabolism. The MTT assay is based on the ability of metabolically active fibroblast cells to use the mitochondrial enzyme succinate dehydrogenase (SDH) to convert yellow water-soluble tetrazolium salt (MTT) into purple formazan crystals. The amount of viable cells determined the intensity of the resulting purple color. After the experiment, 200 μL of MTT solution per milliliter of culture (MTT 5 mg mL dissolved in PBS and filtered

through a 0.2 μm filter before use) was added. The culture was then rinsed with 1× PBS. After three hours of incubation at 37 °C, 300 μL of dimethyl sulfoxide (DMSO) was added to each culture. For thirty minutes, the entire contents were incubated at room temperature until all cells were lysed and a uniform color was achieved. To separate the cell debris, the solution was centrifuged for 2 min. Optical density (OD) was measured at 540 nm using a spectrophotometer. As a control, MTT solution-treated cells were utilized without the sample. This was used to determine the viability percentage. The percentage viability was calculated using the following equation:[39]

$$\text{Percentage viability} = [(\text{OD of test})/(\text{OD of control})] \times 100 \quad (4)$$

2.6.10. *In vitro* drug release and kinetics study. To examine the release of lapatinib from the loaded membranes, the membranes (1.9 cm diameter) were immersed in a simulated intestinal fluid (SIF) solution with a pH of 6.8 (which is also the pH of breast cancer cells) and simulated gastric fluid (SGF) with a pH of 1.2 at 37 ± 2 °C. Aliquots were withdrawn from the release medium at predetermined intervals and quantified using a UV spectrophotometer. A calibration plot was prepared by measuring the UV absorbance of a lapatinib solution of known concentration. The concentration of the drug released during each period was determined using calibration plots. The results are presented in terms of cumulative release as a function of release time. The drug release was compared against free lapatinib under identical conditions. Release experiments were performed in triplicate. Results are reported as mean ± SD. Statistical significance between groups at each time point was assessed using one-way ANOVA, with $p < 0.05$ considered significant. The cumulative drug release percentage was calculated using the following equation:[40]

$$\text{Cumulative release (\%)} = C_t/C_i \times 100 \quad (5)$$

where C_t is the amount of drug released at time 't', and C_i is the total amount of drug in the membrane.

To predict the mechanism of drug release, the cumulative percentage of the drug release profile was fitted with different mathematical equations, as shown in the following equations:[41,42]

Zero-order model,

$$Q_t = Q_0 - K_0 t \quad (6)$$

First-order model,

$$\log Q_t = \log Q_0 - K_1 t/(2.303) \quad (7)$$

Higuchi model,

$$Q_t/Q_o = KH\sqrt{t} \quad (8)$$

Korsmeyer–Peppas model,

$$Q_t/Q_\infty = Kt^n \quad (9)$$

where Q_t is the cumulative drug release at time t (min), Q_0 is the initial amount of drug in the solution, and Q_∞ is the cumulative drug release at an infinite time. K_0, K_1, K_H, and K are the release kinetic constants. The release exponent 'n' proposes the mechanism of drug release.

3. Results and discussion

3.1. Characterization of Zr-MOF and lap-loaded Zr-MOF

3.1.1. X-ray diffraction (XRD) analysis. Fig. 3(a) represents the XRD patterns of Zr-MOF (UiO-66). The characteristic peaks matched those of the previously reported Zr-MOF (UiO-66).[43] The peaks at 2θ = 7.35°, 8.48°, 12.02°, 14.10°, 14.70°, 17.04°, 17.35°, 20.90°, 22.19°, 24.18°, 25.68°, 27.94°, and 29.75° correspond to the planes (111), (002), (022), (113), (004), (133), (024), (004), (135), (244), (444), (117), and (046), respectively. According to the Scherrer equation,[42] the estimated theoretical crystal size was 2.01 nm. Fig. 3(b) shows the XRD pattern of lapatinib-loaded Zr-MOF. Table 1 lists the sample codes for the lapatinib-loaded Zr-MOFs. Key reflections are at 2θ = 18.64°, 21.03°, 23.08°, 24.28°, 25.39°, 28.20°, 29.85°, and 30.74°. The figure also shows the main peaks of Zr-MOF (UiO-66), as shown in Fig. 3(a). Fig. 3(c) shows the XRD pattern of pure lapatinib. Due to its strong crystalline structure, the XRD pattern of lapatinib exhibited distinctive peaks at 2θ values of 6.82°, 8.40°, 11.65°, 12.12°, 12.68°, 14.65°, 16.00°, 16.90°, 17,48°, 18.32°, 20.71°, 21.37°, 22.66°, 23.10°, 24.10°, 25.60°, 27.59°, 28.30°, and 29.25°.[44,45]

3.1.2. Fourier transform infrared (FTIR) analysis. Fig. 4(a) shows the FTIR spectrum of Zr-MOF. It displays absorption peaks associated with the symmetric and asymmetric stretching vibrations of C═O–O carboxylate groups from terephthalic acid at 1400 and 1580 cm^{-1}. Additionally, a broad band at 3400 cm^{-1} indicates the OH stretching vibrations, likely due to water molecules being closely bound, possibly originating from zirconium oxychloride octahydrate. Additionally, the peak at 749 cm^{-1} in the O–Zr–O stretching vibrations suggests the formation of an octahedral zirconium oxide cluster. Furthermore, the Zr–O–C stretching vibrations at 550 cm^{-1} indicate the bridging between the carboxylate groups of the terephthalic acid and zirconium oxide cluster. These findings align well with previous reports confirming the successful synthesis of Zr-MOF (UiO-66).[46] Fig. 4 (b) shows the FTIR spectra of lapatinib and lapatinib-loaded Zr-MOF with different weight percentages (20%, 30%, 40%, and 50%). The peaks observed at 542 cm^{-1}, 743 cm^{-1}, 1134 cm^{-1}, 1500–1600 cm^{-1}, 1585–1600 cm^{-1}, and 1350–1470 cm^{-1} are associated with Zr–O–C, O–Zr–O, C–SO_2, C═C in the benzene ring,C–C in the ring, and C═N, respectively, confirming the presence of the drug. The small broad peak observed at 3300–3400 cm^{-1} can be attributed to the presence of the N–H group of lapatinib.

3.1.3. Thermogravimetric analysis (TGA). Fig. 5(a) shows the TGA plot of Zr-MOF. It reflects high thermal stability, with a decomposition temperature of 540 °C. The inorganic unit of Zr-MOF is key to its superior stability. Zr-MOFs experienced a three-stage weight loss process. The initial 15% weight loss at approximately 200 °C-373 °C is attributed to the evaporation of surface-adsorbed water on Zr-MOFs. The second weight loss of approximately 35% was observed at 473–593 °C, which is linked

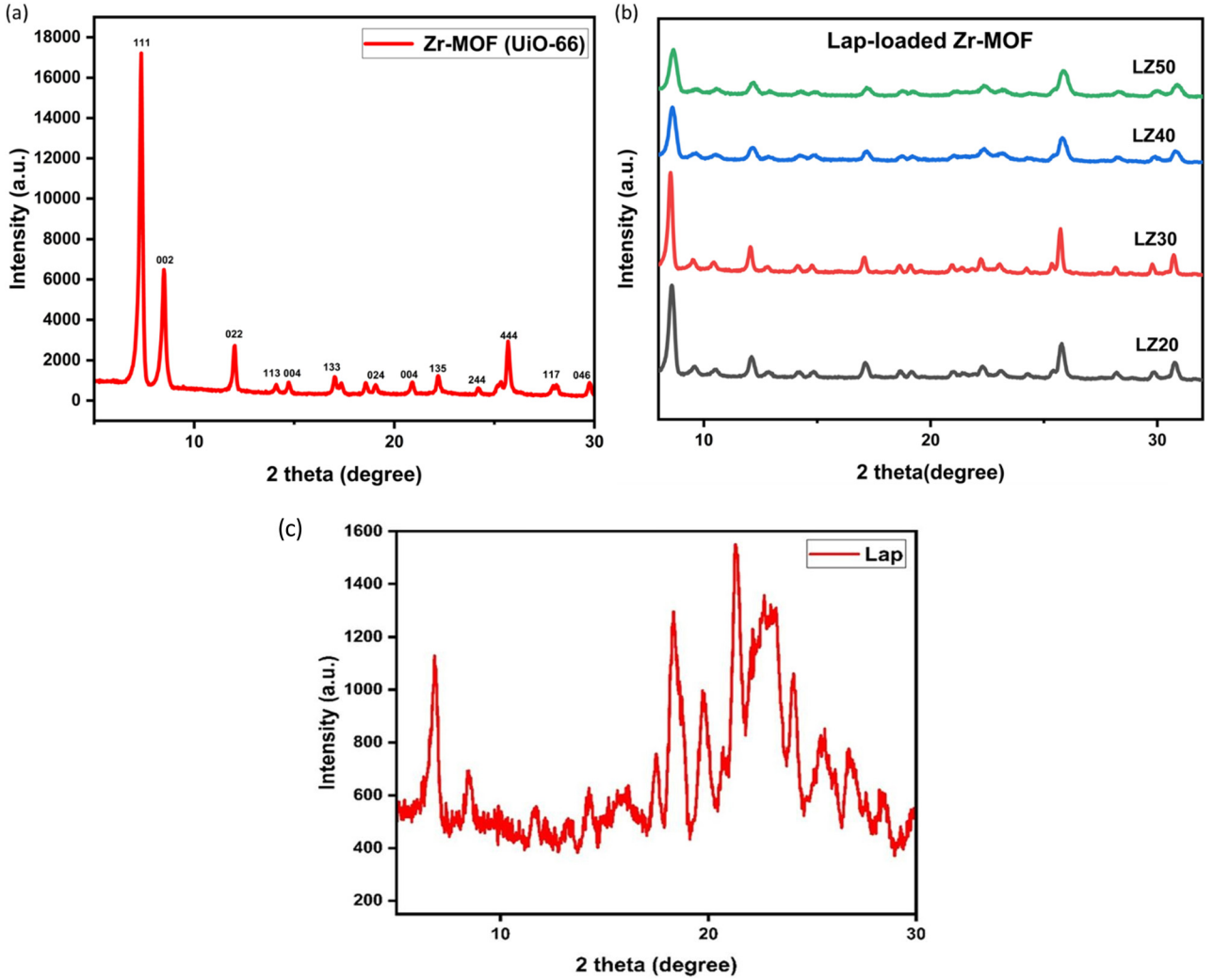

Fig. 3 XRD patterns of: (a) Zr-MOF (UiO-66), (b) lapatinib-loaded Zr-MOF (LZ20, LZ30, LZ40, and LZ50 for 20, 30, 40, and 50 weight percent (wt%) of lapatinib, respectively), and (c) pure lapatinib.

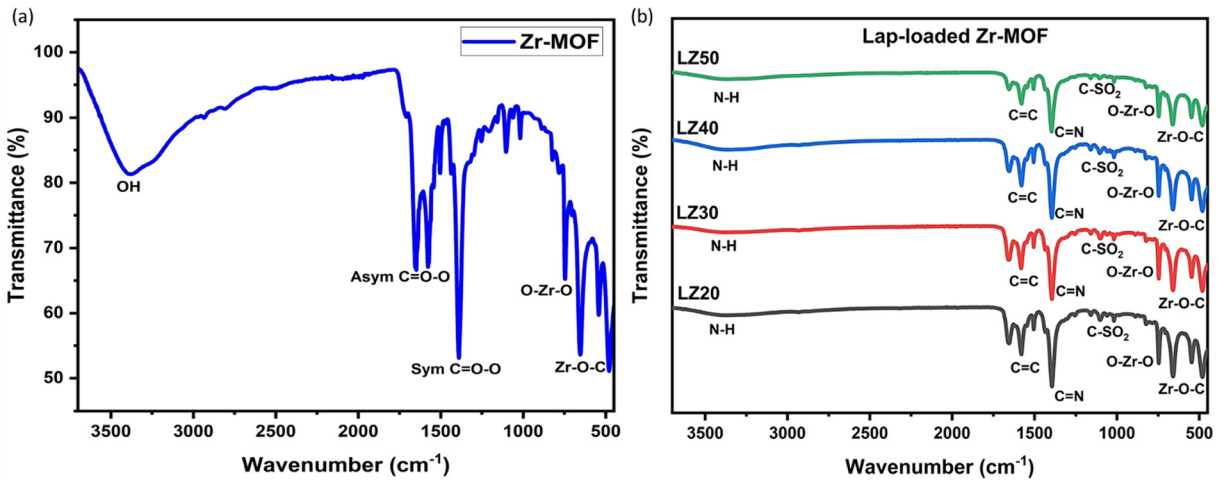

Fig. 4 FTIR spectra of: (a) Zr-MOF and (b) lapatinib-loaded Zr-MOF (LZ20, LZ30, LZ40, and LZ50 for 20, 30, 40, and 50 weight percent (wt%) of lapatinib, respectively).

to the decomposition of the DMF solvent when tested separately. Finally, the third stage of weight loss, which occurs at 723–833 °C, is ascribed to the decomposition of Zr-MOF into ZrO_2. Fig. 5(b) shows the TGA plot of the lapatinib-loaded Zr-MOF at different weight percentages (20%, 30%, 40%, and 50%). The Initial weight loss up to 110 °C may be due to moisture loss. The weight loss between 150–250 °C can be attributed to the decomposition of lapatinib. The net weight loss between 350–550 °C can be attributed to the decomposition of the organic linker in Zr-MOF. After 550 °C, the weight loss can be attributed to the decomposition of the inorganic unit ZrO_2. The thermal stability of the sample was found to be approximately 200 °C. Fig. 5(b) shows weight losses of 18.2% (LZ20), 28.7% (LZ30), 38.1%(LZ40), and 47.3%(LZ50) in the 150–250 °C range, matching the theoretical drug loading. This confirms the quantitative encapsulation and degradation of lapatinib in its pure form, indicating pore confinement rather than surface adsorption. The precise agreement between the TGA weight loss and drug loading percentage rules out significant surface adsorption, as the free drug would degrade below 150 °C. The Zr-MOF's pore structure thus protects lapatinib until its intrinsic decomposition temperature.

3.1.4. Surface morphology analysis. Fig. 6 shows the scanning electron microscopy (SEM) images of the optimized samples. Fig. 6(a) shows the SEM image of Zr-MOF (UiO-66), and Fig. 6(b) shows that of lapatinib-loaded Zr-MOF. Well-defined cubic-like crystals of Zr-MOF (UiO-66) were obtained in compliance with the literature.[47] Particle size has been calculated with the help of the ImageJ software and is 783 nm. The SEM image of the lapatinib-loaded Zr-MOF shows a slight deformation in its structure due to drug loading. The uneven texture indicates drug entrapment within the pores. The drug molecule occupies the porous framework of the Zr-MOF, leading to localized stress and strain in the MOF structure. This leads to edge rounding and asymmetry. The particle size was approximately 700 nm.

Fig. 7(a) shows transmission electron microscopy (TEM) images of the Zr-MOF (UiO-66), revealing uniform, well-defined nanoparticles with a predominantly cubic morphology. The average particle size has been estimated to be approximately 200 nm, which is consistent with previously reported values for UiO-66.[48] The nanocrystals exhibited smooth surfaces and sharp edges, indicating high crystallinity. The well-dispersed nanoparticles, with minimal aggregation observed in the micrographs, suggest strong colloidal stability under the conditions used for sample preparation. Fig. 7(b) shows the TEM image of lapatinib-loaded Zr-MOF. After loading with lapatinib, the morphological features of the Zr-MOF particles remained largely unchanged. The lapatinib-loaded Zr-MOF exhibited a regular cubic-like morphology and a size distribution similar to that of the unloaded counterpart, indicating that the drug loading process did not cause significant structural deformation or aggregation. However, slight variations in surface contrast and a minor increase in particle surface roughness have been apparent, which can be attributed to the presence of drug molecules either encapsulated within the pores or adsorbed onto the MOF surface. The observed structural stability suggests that the Zr-MOF framework is sufficiently robust to accommodate lapatinib without collapse or aggregation, which is essential for efficient drug release under varying pH conditions. Enhanced surface roughness and changes in the TEM contrast may also corroborate successful drug encapsulation.[49]

3.1.5. Brunauer Emmett Teller (BET) analysis. Fig. 8(a) and (b) show the Brunauer–Emmett–Teller (BET) surface area analysis of Zr-MOF (UiO-66) and lapatinib-loaded Zr-MOF, respectively. The Zr-MOF demonstrated a high specific surface area, typically in the range of 619.92 $m^2\ g^{-1}$, indicating the highly porous nature. The nitrogen adsorption–desorption isotherm exhibited a type I profile, which is characteristic of microporous materials. The average pore diameter is calculated as 1.1543 nm, reflecting the microporous nature. Such pore dimensions enable the encapsulation of drugs within the framework while restricting their

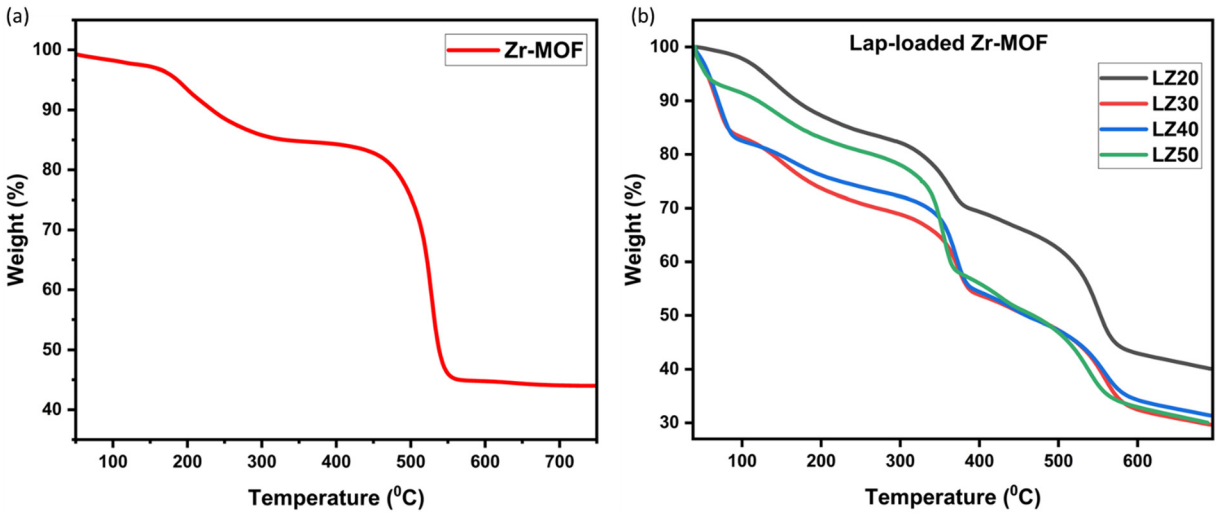

Fig. 5 TGA of: (a) Zr-MOF and (b) lapatinib-loaded Zr-MOF (LZ20, LZ30, LZ40, and LZ50 for 20, 30, 40, and 50 weight percent (wt%) of lapatinib, respectively).

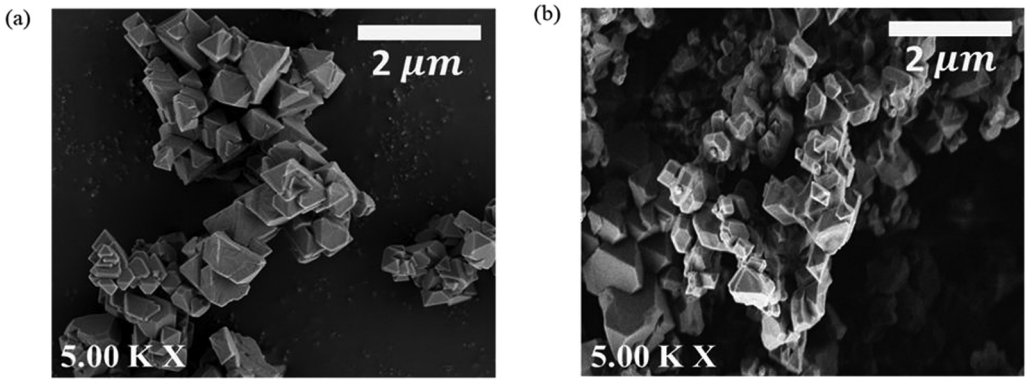

Fig. 6 SEM images of: (a) Zr-MOF (UiO-66) and (b) lapatinib-loaded Zr-MOF.

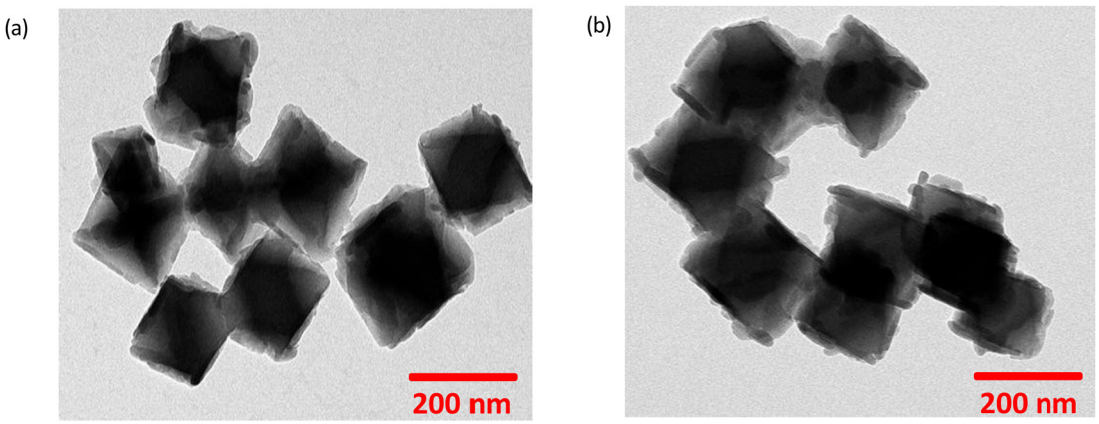

Fig. 7 TEM images of: (a) Zr-MOF (UiO-66) and (b) lapatinib-loaded Zr-MOF.

premature diffusion, allowing for a sustained and controlled release profile. Fig. 8(b) shows the BET analysis result of lapatinib-loaded Zr-MOF. The BET analysis revealed a noticeable reduction in both the specific surface area and total pore volume

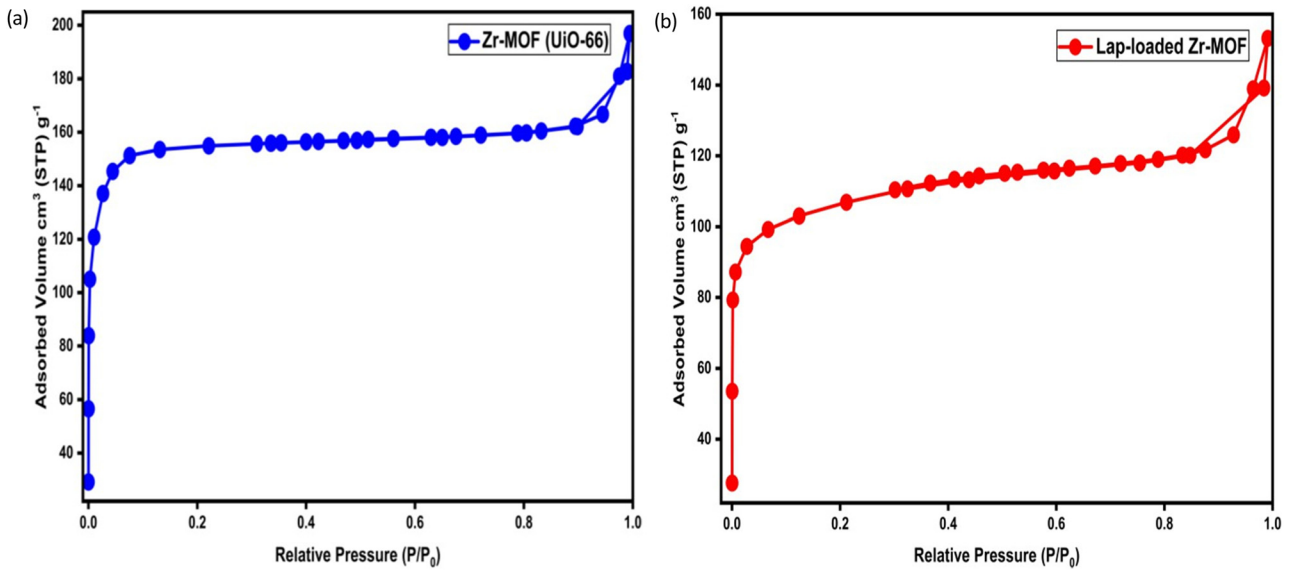

Fig. 8 BET isotherms of: (a) Zr-MOF (UiO-66) and (b) lapatinib-loaded Zr-MOF.

of the Zr-MOF after the drug loading. The surface area decreased to 405.72 $m^2 g^{-1}$, accompanied by a substantial reduction in pore diameter to 0.2853 nm. The isotherms retained a similar profile, suggesting that the overall framework structure of the MOF remained intact post-loading. The observed decrease in porosity provides further evidence for the successful encapsulation of lapatinib within the MOF framework rather than simple surface adsorption. This encapsulation is crucial for achieving a controlled pH-responsive drug release, as the drug's location within the MOF's microporous structure can protect it from premature release and enable stimuli-responsive release behavior.[50]

3.2. Characterization of SA/PVP blends and SA/PVP/Lap-Zr-MOF

3.2.1. XRD analysis. Fig. 9(a) shows the XRD peaks of the SA/PVP blend, and Fig. 9(b) shows the XRD patterns of SA/PVP/Lap-loaded Zr-MOF with different weight percentages of lapatinib-loaded Zr-MOF. The SA/PVP blend exhibited a predominant amorphous nature. The 2θ values of 18.76°, 22.57°, 23.57°, and 2.59° correspond to the SA/PVP film. This result is consistent with that of a previous study.[51] The XRD pattern of the SA/PVP/Lap-loaded Zr-MOF shows sharp peaks for Zr-MOF, indicating that a stable framework was maintained. Broad amorphous peaks were observed, indicating the amorphous nature of SA/PVP. No additional crystalline peaks were observed for the free drug, indicating no drug leakage or phase separation. This confirms the homogeneous film formation with well-dispersed MOF and effective drug loading into MOF pores.

3.2.2. FTIR analysis. Fig. 10(a) shows the FTIR spectra of the SA/PVP films with different weight ratios (SA : PVP as 90 : 10, 80 : 20, and 70 : 30), and Fig. 10(b) shows the FTIR spectra of SA/PVP/Lap-loaded Zr-MOF with different weight percentages (5%, 10%, 15%, and 20%). In the spectra of SA/PVP, PVP, and SA, which are hydrophilic, hydroxylic peaks were observed at approximately 3430 cm^{-1}. The peak at 2926 cm^{-1} is attributed to the asymmetric stretching vibration of the –CH in the skeletal chain of PVP. The vibration absorption of the C–N bond is represented by a peak at 1291 cm^{-1}. The stretching vibration of C=O in PVP is indicated by a peak at 1632 cm^{-1}. The C–N stretching can be observed at 1168 cm^{-1}. The C–C vibration is represented by a peak at 1419 cm^{-1}. A peak at 1025 cm^{-1} corresponds to the stretching vibration of the ether bond (C–O–C aliphatic), confirming the formation of the SA/PVP film.[52] In the FTIR spectrum of SA/PVP/Lap-Zr-MOF, a peak was observed at 3400 cm^{-1}, corresponding to hydrogen bonding. The –CH bonding is indicated at 2934 cm^{-1}, and the C=O bond is represented at 1648 cm^{-1}. Peaks for the C–C, C–N, and C–O bonds were observed at 1407 cm^{-1}, 1074 cm^{-1}, and 1024 cm^{-1}, respectively. The main peaks for Zr-MOF were observed at 566 cm^{-1} and 816 cm^{-1}, which were attributed to Zr–O–C and O–Zr–O, respectively.

3.2.3. TGA. Fig. 11(a) shows the TGA plot of the SA/PVP film, and Fig. 11(b) shows the TGA plot of the SA/PVP/Lap-loaded Zr-MOF with different weight percentages. For the SA/PVP film, a 20% weight loss observed up to 150 °C indicates the evaporation of moisture. The weight loss from 190–250 °C may be due to the decomposition of PVP and SA. Between 200 °C and 300 °C the weight loss is due to the residual carbonization of the organic fragment. The major stable residue was observed above 300 °C. The thermal stability of the SA/PVP blend was approximately 180–240 °C. In the TGA plot of SA/PVP/Lap-loaded Zr-MOF, the initial weight loss up to 190 °C might be due to moisture loss and decomposition of PVP. Weight loss up to 230 °C is due to the decomposition of SA. Another weight loss observed up to 350–450 °C may be due to the decomposition of Zr-MOF. The TGA results confirmed thermal stability at body temperature, indicating that the system degraded in a controlled manner under physiological pH conditions. This ensures that the drug remains protected until it reaches the target site. The TGA curves of SPLZ5 and SPLZ10 exhibited minor weight losses at approximately 200 °C, which was attributed to the PVP decomposition in the SA/PVP matrix. This peak diminished in the higher-loading composites because of

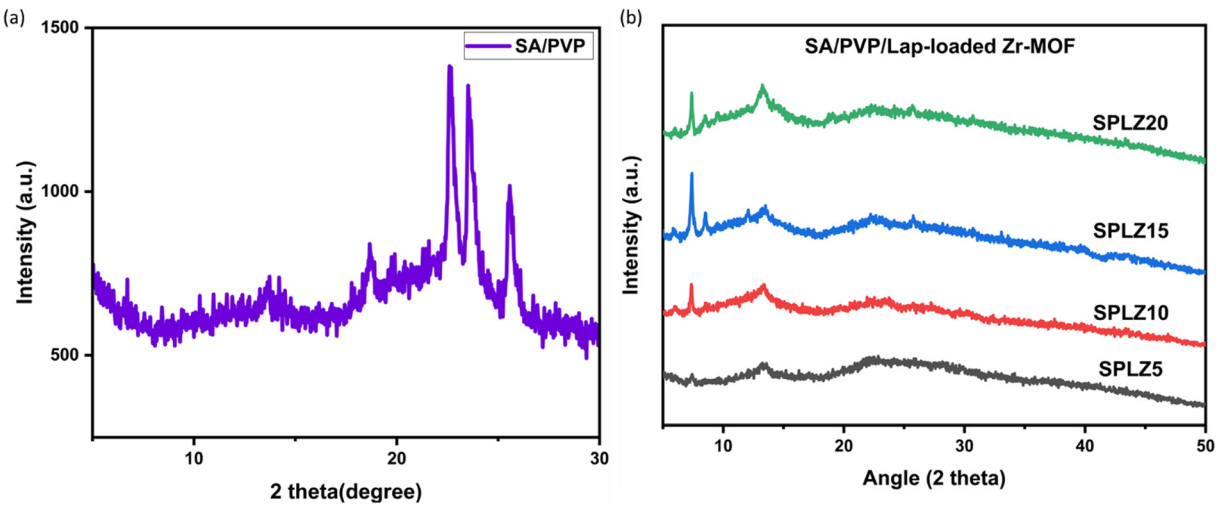

Fig. 9 XRD patterns of: (a) SA/PVP film and (b) SA/PVP/Lap-loaded Zr-MOF samples (5%, 10%, 15%, and 20% of lapatinib-loaded Zr-MOF with the optimized SA/PVP blend (90 : 10 SA/PVP), labelled as SPLZ5, SPLZ10, SPLZ15, and SPLZ20, respectively).

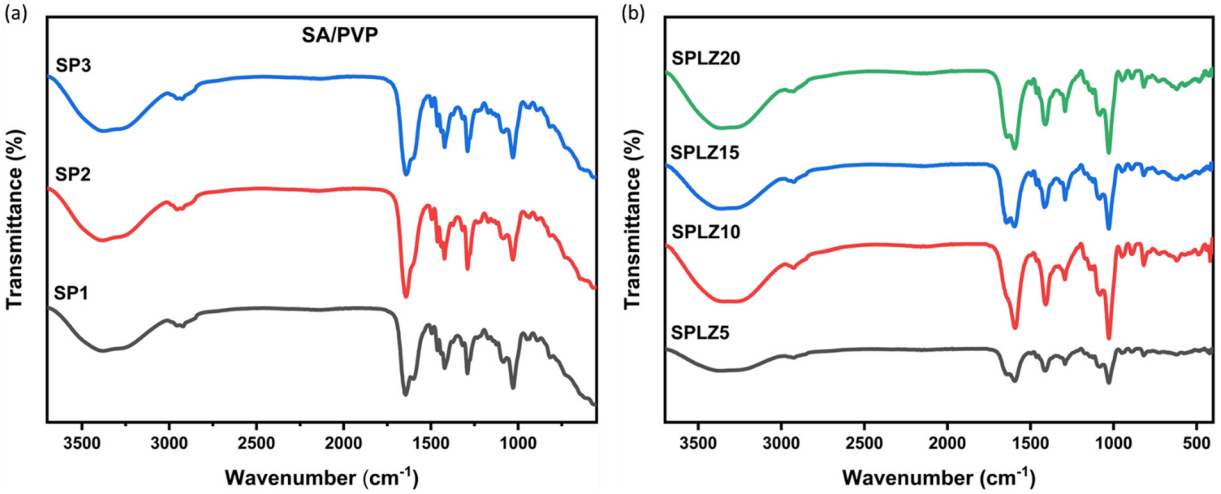

Fig. 10 FTIR spectra of: (a) SA/PVP films with different weight percentage ratios (90 : 10, 80 : 20, 70 : 30) and (b) SA/PVP/Lap-loaded Zr-MOF with different weight percentages (5%, 10%, 15%, and 20% of lapatinib-loaded Zr-MOF with the optimized SA/PVP blend (90 : 10 SA/PVP), labelled as SPLZ5, SPLZ10, SPLZ15, and SPLZ20, respectively).

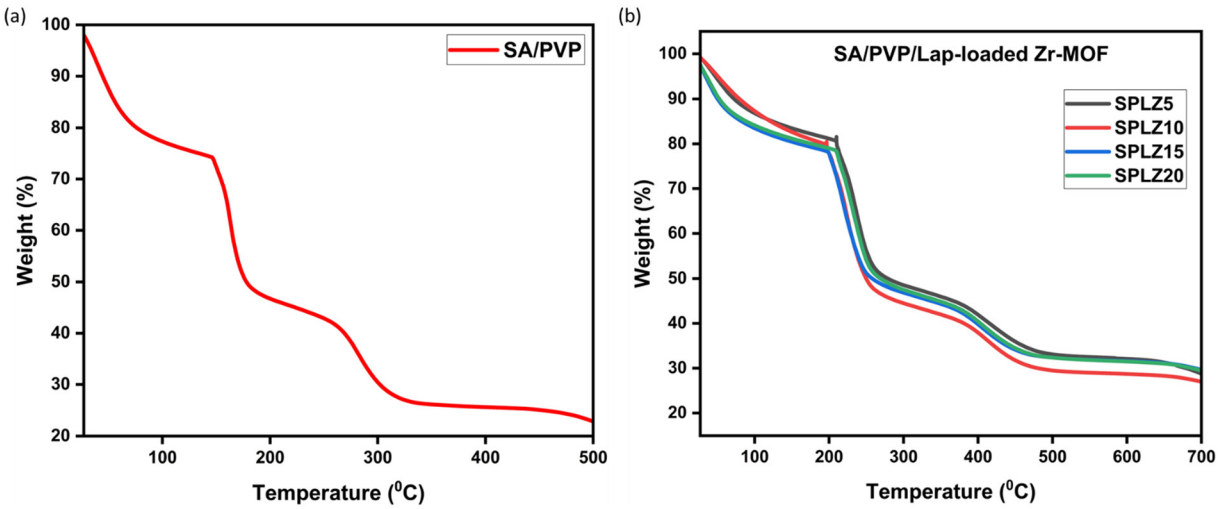

Fig. 11 TGA of: (a) optimized SA/PVP film (90 : 10) and (b) different weight percentages of SA/PVP/Lap-loaded Zr-MOF (5%, 10%, 15%, and 20% of lapatinib-loaded Zr-MOF with the optimized SA/PVP blend (90 : 10 SA/PVP), labelled as SPLZ5, SPLZ10, SPLZ15, and SPLZ20, respectively).

the dominant thermal responses of lapatinib and alginate. At 5–10% loading, PVP may form localized domains that degrade independently, whereas at higher loadings, stronger interfacial interactions with lapatinib-Zr-MOF suppress this effect.

3.2.4. Mechanical properties. Fig. 12(a)–(d) show the percentage elongation, tensile strength, Young's modulus, and stress–strain plot of the SA/PVP films (SA : PVP 90 : 10, 80 : 20, and 70 : 30). The percentage elongation reflects the ability of a material to stretch or elongate before it breaks. The 90 : 10 SA/PVP film exhibited the highest percentage elongation, indicating that the film was more ductile and capable of significant stretching before fracture. As the ratio shifted to 80 : 20 and 70 : 30, the percentage elongation decreased, making the film less capable of elongation. A higher proportion of SA likely provides a balance between strength and flexibility at a 90 : 10 ratio. Tensile strength is the maximum stress that a material can withstand while being stretched or pulled before breaking. The 90 : 10 SA/PVP system exhibited the highest tensile strength, followed by the 80 : 20 and 70 : 30 systems. This indicates that films with higher SA contents (such as 90 : 10) are more resistant to breaking under tension than those with lower SA contents (70 : 30 ratio). The Young's modulus, which is a measure of the derivative of stress and strain, was also higher for the 90 : 10 SA/PVP system. Based on these results, the 90 : 10 SA/PVP system was identified as the optimal system for practical applications.

In Fig. 13(a)–(d) represent percentage elongation, tensile strength, Young's modulus, and stress–strain plots of SA/PVP/Lap-Zr-MOF, respectively, with different weight percentages (5%, 10%, 15%, and 20%). Among the composite films, the 20% SA/PVP/Lap-loaded Zr-MOF formulation exhibited the

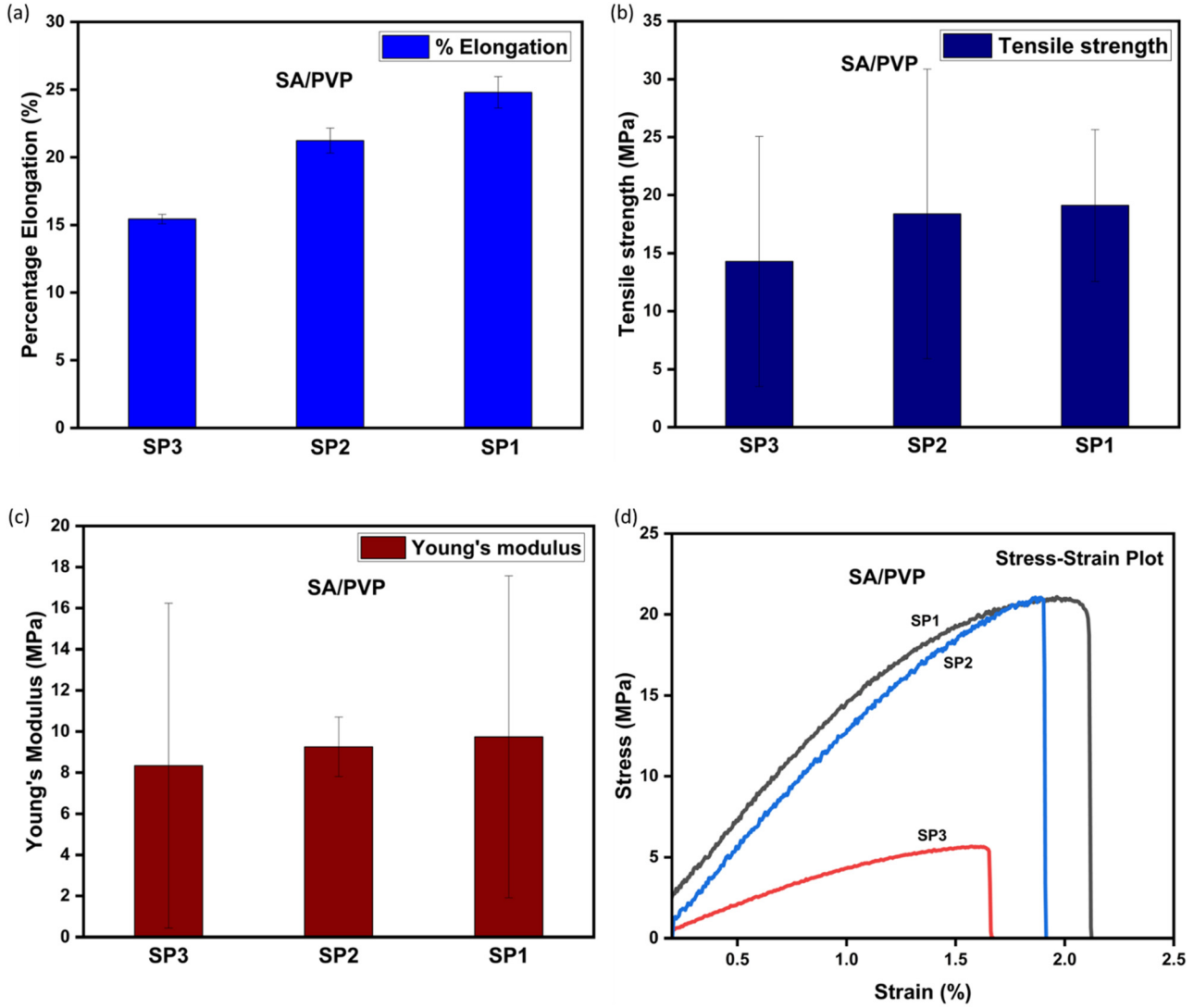

Fig. 12 (a) Percentage elongation of SA/PVP films, (b) tensile strength of SA/PVP films, (c) Young's modulus of SA/PVP films, and (d) stress–strain plot of SA-PVP films (weight percentages of 90%, 80%, and 70% SA and 10%, 20%, and 30% PVP, labelled as SP1, SP2, and SP3).

highest tensile strength, percentage elongation, and Young's modulus compared to the 5%, 10%, and 15% loaded formulations. This suggests that at 20% loading, the Zr-MOF particles provide optimal reinforcement to the SA/PVP matrix, improving the stiffness (Young's modulus) while maintaining flexibility (% elongation). Lower loadings (5–15%) likely suffer from incomplete dispersion or insufficient filler-matrix interactions, resulting in inferior mechanical performance.

The pure SA/PVP blend exhibited a higher tensile strength than all the composite films. This is attributed to the uninterrupted hydrogen-bonded polymer network of SA/PVP, which distributes stress more efficiently than the network of the composite films containing rigid Zr-MOF particles. However, the percentage elongation of the SA/PVP/Lap-loaded Zr-MOF films exceeded that of the pure SA/PVP films. This indicates that the incorporation of drug-loaded Zr-MOF introduces a degree of plasticity, likely due to a reduced polymer chain packing density around the MOF particles, which enhances the ductility or microstructural rearrangements induced by the MOF-polymer interface, allowing for greater deformation before the fracture. For oral drug delivery, the percentage elongation is a critical parameter that reflects the ability of a material to withstand mechanical stress during swallowing, gastric motility, and intestinal transit, without fracturing. The enhanced elongation of the composites suggests superior flexibility and durability under physiological conditions, making them more suitable for applications involving gastrointestinal drug release. The 20% SA/PVP/Lap-loaded Zr-MOF formulation, with its balanced tensile strength and elongation, emerged as the optimal candidate for further development as a pH-responsive lapatinib delivery system. Prior SA/PVP composites or other nanoparticle-polymer systems often sacrifice their flexibility when the filler content is increased.[53] Mechanically, our optimized films (particularly at 20% loading) demonstrated improved tensile strength and elongation compared to lower loadings and maintained greater flexibility than pure MOF or nonreinforced polymer films.

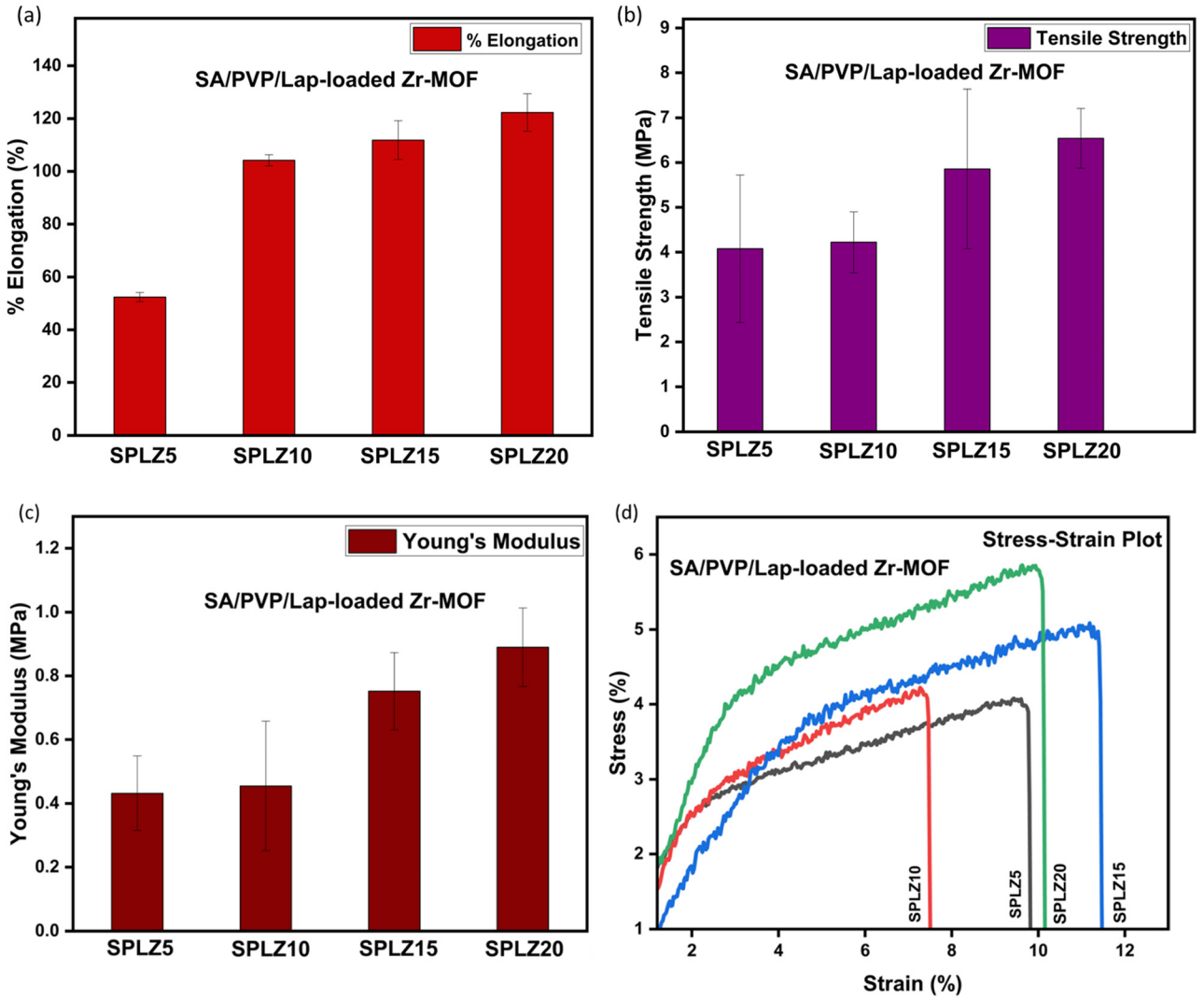

Fig. 13 (a)–(d) represent percentage elongation, tensile strength, Young's modulus, and stress–strain plot of SA/PVP/Lap-loaded Zr-MOF, respectively (5%, 10%, 15%, and 20% of lapatinib-loaded Zr-MOF with the optimized SA/PVP blend (90 : 10 SA/PVP), labelled as SPLZ5, SPLZ10, SPLZ15, and SPLZ20, respectively).

3.2.5. Surface wettability. The water contact angle is a measure of the wettability of a surface. A lower contact angle ($<90^{\circ}$) indicates a more hydrophilic surface, such that water spreads out more easily on the surface. Conversely, a higher contact angle ($>90^{\circ}$) suggests a more hydrophobic surface, where water beads up and does not spread easily. Fig. 14(a) shows the water contact angles of the SA/PVP films with different weight ratios (90 : 10, 80 : 20, and 70 : 30). As the PVP content increased, the water contact angle decreased, indicating an increase in surface hydrophilicity. Both SA and PVP are hydrophilic polymers. However, when PVP is mixed with a combined polymer matrix, it tends to make the surface more hydrophilic than SA. The 90 : 10 SA/PVP ratio can be considered the ideal formulation for drug delivery because it offers an optimal balance of the properties required for a controlled and sustained drug release. While a more hydrophilic surface facilitates faster water uptake and drug release, a slightly hydrophobic character can slow down the release, ensuring a more controlled and sustained release profile. Fig. 14(b) shows the water contact angles of SA/PVP/Lap-Zr-MOF with different weight percentages (5, 10, 15, and 20%). The highest water contact angle was observed for the 20% SA/PVP/Lap-Zr-MOF, followed by the 15%, 10%, and 5% formulations, respectively. This indicates that as the percentage of lapatinib-loaded Zr-MOF in the SA/PVP matrix increased, the surface became less hydrophilic. Lapatinib is a hydrophobic drug, which means that as its loading increases, the hydrophobicity of the film surface increases. The 20% SA/PVP/Lap-Zr-MOF film is more likely to provide a slower, controlled release of the drug, whereas the 5% formulation might release the drug more quickly because of greater interaction with water.

3.2.6. Surface morphology analysis. Fig. 15(a) shows an SEM image of the optimized 90 : 10 SA/PVP film. A relatively smooth and homogeneous characterization was obtained. No visible cracks were observed during phase separation, indicating good compatibility between SA and PVP. The uniform morphology suggests strong hydrogen bonding and good

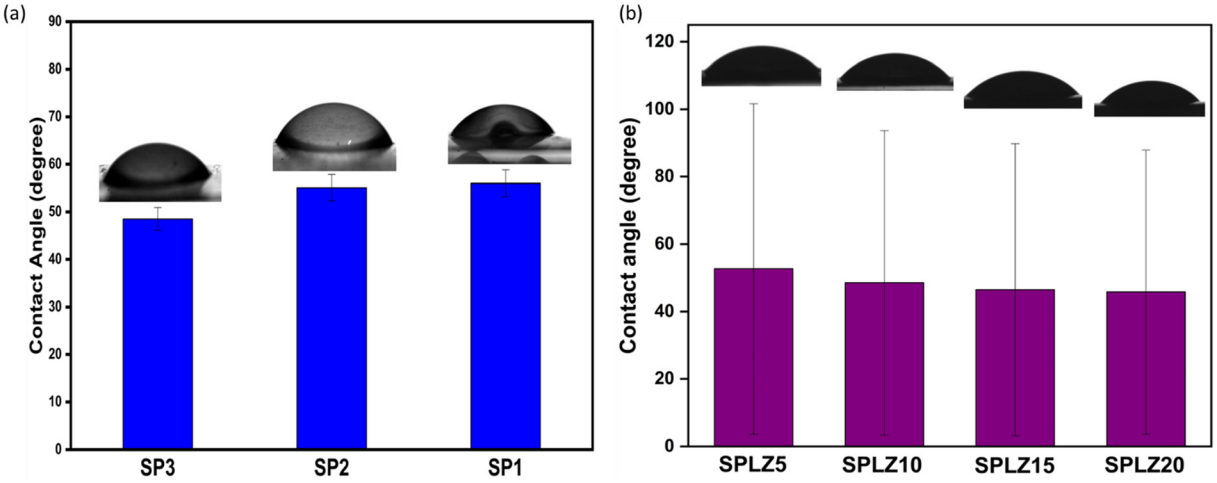

Fig. 14 Water contact angle measurements of (a) SA/PVP films with different weight percentage ratios (90 : 10, 80 : 20, and 70 : 30) and (b) SA/PVP/Lap-Zr-MOF with different weight percentages (5%, 10%, 15%, and 20%).

film-forming properties. Fig. 15(b) shows the SEM image of the SA/PVP/Lap-loaded Zr-MOF, which reflects the distribution of Zr-MOF within the polymer matrix. It shows a continuous dense film with sporadic, small angular particles. No large cracks or voids were observed, indicating good film formation. A slight surface roughness compared to the SA/PVP film was observed owing to the drug-loaded MOF protrusions. These morphological features are critical for ensuring the durability of the film during oral drug administration and controlled drug release.[54]

3.2.7. Moisture uptake and swelling ratio. Table 4 lists the moisture uptake and swelling ratios of the SA/PVP and SA/PVP/Lap-Zr-MOF samples. The SA/PVP films exhibited slightly higher moisture uptake and swelling ratios than the SA/PVP/Lap-Zr-MOF samples. This is due to the dominant hydrophilic nature of SA and PVP polymers. The incorporation of lapatinib-loaded Zr-MOF into the polymer matrix decreased hydrophilicity and increased structural integrity. The relatively low moisture uptake of SA/PVP/Lap-Zr-MOF indicates that the film has an intrinsic ability to limit excessive hydration, which can lead to premature drug release. This is particularly important for lapatinib, a hydrophobic drug, because moisture uptake must be controlled to avoid rapid drug release or instability in moist environments. A swelling ratio of approximately 200% indicates a moderate degree of water absorption by the film, which is essential for drug delivery. In drug delivery systems, swelling allows the film to absorb bodily fluids, creating a pathway for the controlled release of the drug.[55] The lower swelling ratio of the drug-loaded MOF sample compared to SA/PVP suggests that the film will release the drug more slowly and over an extended period, which is often desirable in cancer treatment to maintain sustained therapeutic levels of the drug in the body. The incorporation of Zr-MOF enhanced the mechanical stability of the film, preventing excessive swelling that could cause premature disintegration or burst release of the drug. This ensures that the film remains intact long enough to release the drug at a controlled rate, rather than a rapid, uncontrolled burst that could lead to toxicity or suboptimal treatment. The combination of approximately 15% moisture uptake and 200% swelling ratio is well-suited for oral delivery, facilitating gradual drug ingress and sustained bioavailability, as highlighted in studies on composite systems.[56]

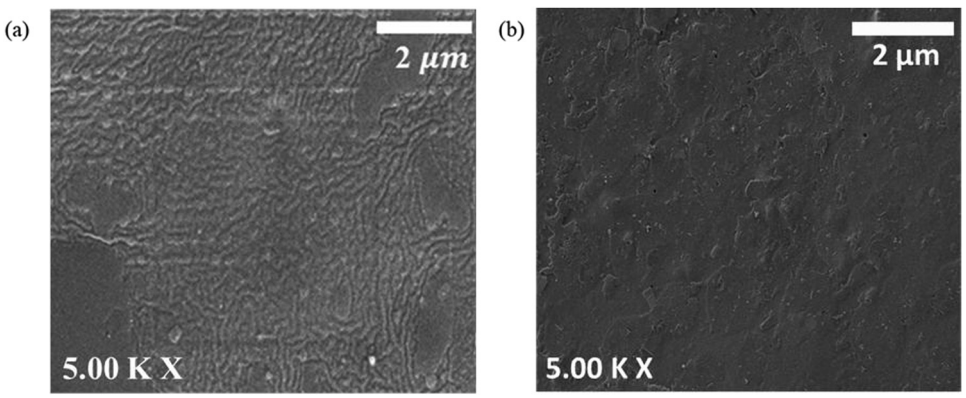

Fig. 15 SEM image of (a) SA/PVP film and (b) SA/PVP/Lap-Zr-MOF.

Table 4 Moisture uptake and swelling ratio percentages of SA/PVP and SA/PVP/Lap-Zr-MOF films (all data are expressed as mean ± SD (n = 3))

Sample code	Moisture uptake (%)	Swelling ratio (%)
SA/PVP	20.3625 ± 0.89	210.43 ± 1.50
SA/PVP/Lap-Zr-MOF	15.8539 ± 1.79[a]	200.99 ± 0.75[a]

[a] indicates a statistically significant difference compared to the control ($p < 0.05$)

3.2.8. *In vitro* biocompatibility evaluation

3.2.8.1. In vitro hemocompatibility analysis. Hemocompatibility analysis is the evaluation of how a material or biomedical device interacts with blood, assessing its safety and compatibility when in contact with blood components.[57] Hemocompatibility tests typically assess hemolysis, which measures the rupture of red blood cells and the release of hemoglobin (Hb). Low hemolysis percentages indicate that the material does not cause significant damage to blood cells. Percentage hemolysis refers to the percentage of red blood cells that are lysed when exposed to a substance or material, releasing hemoglobin into the surrounding medium. It is used as an indicator of the hemocompatibility of a material or drug delivery system, which is crucial for assessing the potential for blood-related toxicity. A hemolysis percentage below 5% is generally considered acceptable and indicates good hemocompatibility, indicating that the material or drug is safe for blood-contact applications.[58] Fig. 16 shows the *in vitro* hemolysis percentage of SA/PVP/lapatinib-loaded Zr-MOF. The average percentage hemolysis was 0.03 ± 0.00 for SA/PVP/lapatinib-loaded Zr-MOF, which was significantly lower than that of the control group (0.05 ± 0.01%, $p < 0.05$, one-way ANOVA), confirming excellent hemocompatibility. This indicates that the system has extremely low hemolytic activity and does not damage RBCs. The low hemolysis percentage also suggests excellent biocompatibility and safety for blood-contacting applications and confirms that it is unlikely to induce toxicity or immune reactions related to the destruction of RBCs. Thus, this system is a promising material for controlled and targeted drug delivery in cancer treatment, as it can safely interact with blood and deliver therapeutic agents without causing adverse effects related to hemolysis.

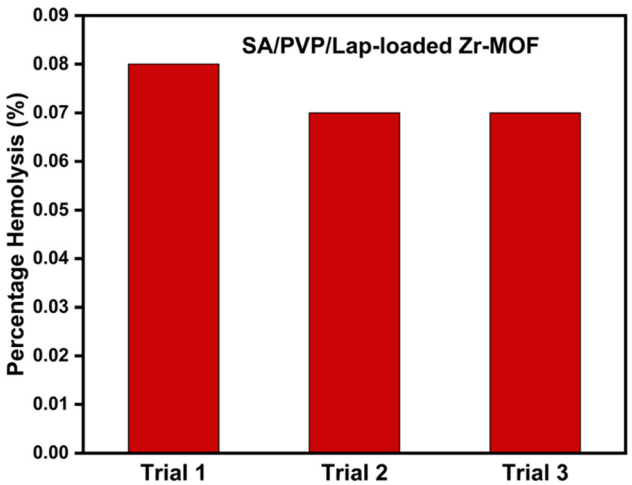

Fig. 16 *In vitro* percentage hemolysis of SA/PVP/Lapatinib-loaded Zr-MOF.

Table 5 Optical density values and cell viability percentage of the control sample and SA/PVP/Lap-Zr-MOF. (All values are mean ± SD (n = 3). $p < 0.05$ *vs.* control)

SAMPLES	OD value I	OD value II	OD value III	OD value (540 nm)	% viability
Control	0.9383	0.9257	0.9218	0.9286	100.00 ± 0.58
SA/PVP/Lap-Zr-MOF	0.8925	0.8748	0.8701	0.8633	94.24 ± 0.86

3.2.8.2. Cytotoxicity evaluation. Cytotoxicity examination is an important method for evaluating cell and tissue responses. Cell cytotoxicity is determined by cell lysis (death) or inhibition of cell proliferation. This evaluation is a crucial step in determining the biocompatibility and safety of materials intended for biomedical applications. Cytotoxicity tests typically measure cell viability, which refers to the percentage of live cells after exposure to a material.[59] We used the MTT assay to measure cell viability, which measures mitochondrial activity that correlates with the number of viable cells. The direct contact assay method was used, in which the cells were directly exposed to the test material, and the effects on cell viability and morphology were assessed. Table 5 shows the optical density (OD) values and calculated cell viability percentage. The system (SA/PVP/Lap-loaded Zr-MOF) exhibited a cell viability of 94.24%. This is important because, while the system is designed to deliver the anti-cancer drug lapatinib to target cancer cells, it should not harm healthy cells. A 94.24% cell viability suggests minimal cytotoxicity to healthy tissue, which is a positive indicator of safety for biomedical applications. Fig. 17 shows the morphology of L929 (Mouse Fibroblast) cells over the SA/PVP/Lap-loaded Zr-MOF sample, observed using a phase-contrast microscope. The spindle-shaped morphology of the cells was retained even after 24 h of incubation, indicating the cell viability of the system. Most MOFs and some PVP-based formulations have been reported to exhibit cytotoxic side effects, with cell viability consistently failing to exceed a certain limit.[60] Our composite achieved 94.2% cell viability, directly supporting its safety.

3.2.9. *In vitro* drug release and kinetics study.

Fig. 18 shows a plot of the cumulative lapatinib release percentage at two different pH values: 6.8 (simulated intestinal fluid and breast cancer cells) and 1.2 (simulated gastric fluid). Fig. 18(a) represents SA/PVP/lapatinib-loaded Zr-MOF and Lap at 6.8 pH,

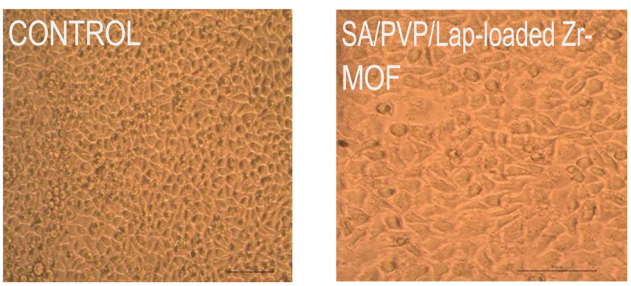

Fig. 17 Phase contrast microscopic images showing the morphology of cells grown on SA/PVP/Lap-loaded Zr-MOF.

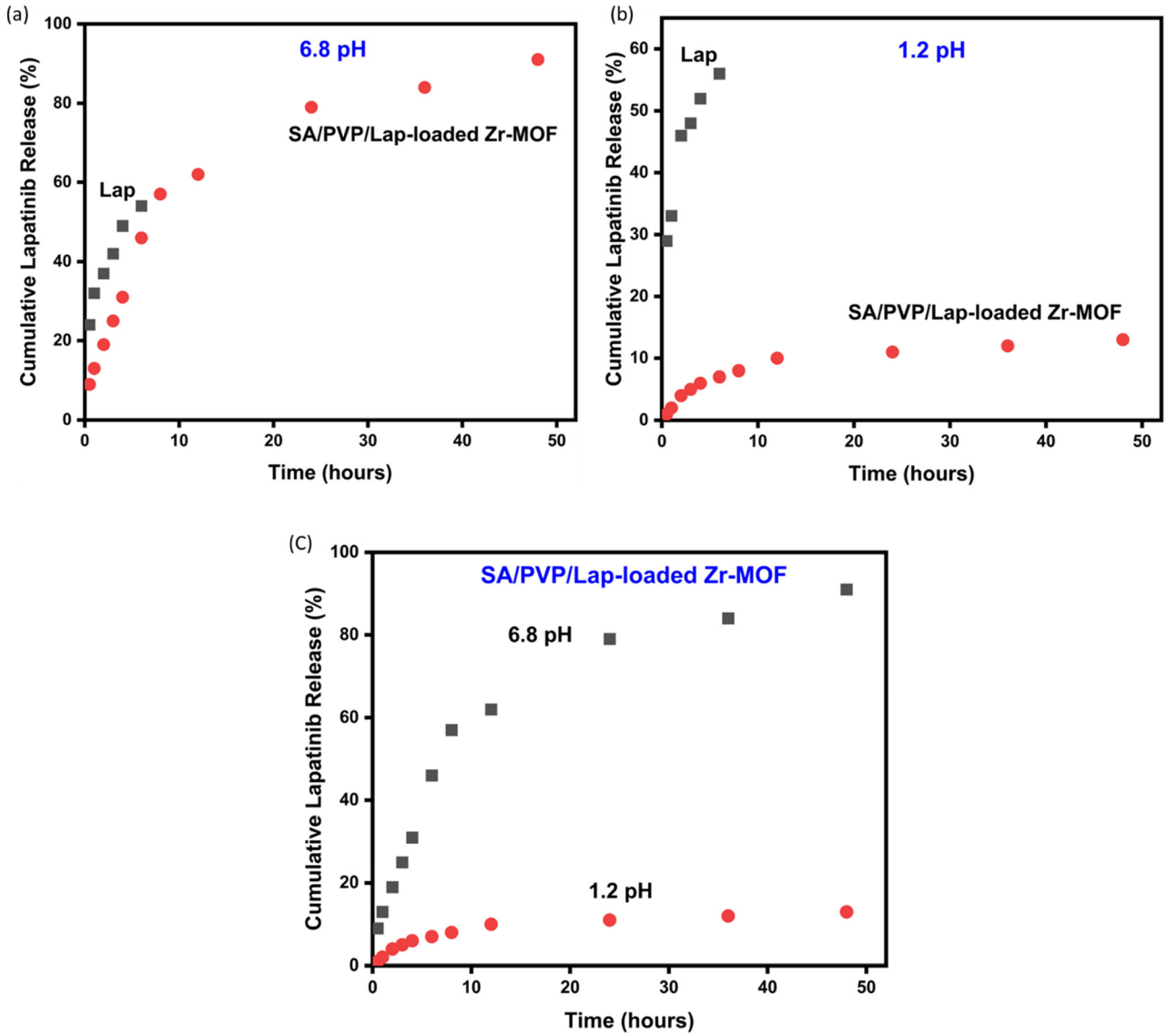

Fig. 18 Cumulative lapatinib release percentage of (a) SA/PVP/lapatinib-loaded Zr-MOF and Lap at 6.8 pH, (b) SA/PVP/lapatinib-loaded Zr-MOF and Lap at 1.2 pH, and (c) SA/PVP/lapatinib-loaded Zr-MOF at 6.8 pH and 1.2 pH.

while Fig. 18(b) represents SA/PVP/lapatinib-loaded Zr-MOF and Lap at 1.2 pH, and Fig. 18(c) represents SA/PVP/lapatinib-loaded Zr-MOF at 6.8 and 1.2 pH. At pH 6.8, lapatinib alone showed a maximum drug release of 54% within 6 h, after which no further drug release was observed. This suggests a relatively fast release but is limited in terms of the total drug that can be delivered over time. The SA/PVP/Lap-Zr-MOF at 6.8 pH showed a sustained release of 91% over 48 h, with drug release continuing for a longer duration and achieving a much higher release percentage compared to lapatinib alone. At pH 1.2, lapatinib alone showed a maximum release of 56% within 6 h, with no further significant release observed. This indicates that the drug is released quickly under acidic conditions but is limited in total release. SA/PVP/Lap-Zr-MOF showed 13% drug release at 1.2 pH over 48 h. This suggests that the release of lapatinib from the MOF was significantly slower and more controlled under acidic conditions.

Fig. 18 shows a plot of the cumulative lapatinib release percentage at two different pH values: 6.8 (simulated intestinal fluid and breast cancer cells) and 1.2 (simulated gastric fluid). Fig. 18(a) represents SA/PVP/lapatinib-loaded Zr-MOF and Lap at 6.8 pH, while Fig. 18(b) represents SA/PVP/lapatinib-loaded Zr-MOF and Lap at 1.2 pH, and Fig. 18(c) represents SA/PVP/lapatinib-loaded Zr-MOF at 6.8 and 1.2 pH. At pH 6.8, lapatinib alone showed a maximum drug release of 54% within 6 h, after which no further drug release was observed. This suggests a relatively fast release but is limited in terms of the total drug that can be delivered over time. The SA/PVP/Lap-Zr-MOF at 6.8 pH showed a sustained release of 91% over 48 h, with drug release continuing for a longer duration and achieving a much higher release percentage compared to lapatinib alone. At pH 1.2, lapatinib alone showed a maximum release of 56% within 6 h, with no further significant release observed. This indicates that the drug is released quickly under acidic conditions but is

limited in total release. SA/PVP/Lap-Zr-MOF showed 13% drug release at 1.2 pH over 48 h. This suggests that the release of lapatinib from the MOF was significantly slower and more controlled under acidic conditions.

Thus, the SA/PVP/Lap-Zr-MOF system demonstrated a sustained and prolonged release of lapatinib at pH 6.8, with 91% release over 48 h. This is highly beneficial for cancer treatment, as it ensures steady drug release over an extended period, potentially improving therapeutic efficiency while reducing the need for frequent dosing. In contrast, lapatinib alone was released more rapidly, reaching only 54% release in 6 h, and offered less control over the release and potentially shorter therapeutic effects. The SA/PVP/Lap-Zr-MOF system showed a significantly reduced drug release of 13% at pH 1.2 (acidic environment) over 48 h. This is the pH of gastric fluids present in the stomach, and the low release observed suggests that the designed MOF system is capable of protecting the drug in acidic environments, preventing premature release before it reaches its target site. Lapatinib alone releases relatively high amounts of approximately 56% at pH 1.2, which could lead to unwanted drug release in the stomach, causing potential side effects and reduced efficacy in reaching the tumor site. The pH-responsive drug release observed for the SA/PVP/Lap-Zr-MOF system *in vitro* suggests its suitability for further exploration as a targeted oral delivery platform in environments resembling the slightly acidic tumor microenvironment (pH 6.8). The enhanced release at pH 6.8, combined with the reduced release observed at pH 1.2, indicates that the system could protect the drug from premature release in the stomach while enabling higher and sustained release once it reaches the tumor site or a neutral-to-slightly acidic environment in the body. Such pH-sensitive drug release characteristics are advantageous for oral drug delivery systems and cancer therapy, as selective release may help maximize efficacy and minimize side effects. At 48 h, the cumulative drug release from the SA/PVP/Lap-Zr-MOF film was 91.01 $\pm$ 1.52%, which was significantly higher than that of lapatinib alone (54.08 $\pm$ 1.52%, $p < 0.05$, one-way ANOVA).

Prior formulations, such as lapatinib-loaded exosomes, polymeric nanoparticles, and PEGylated liposomes, mostly suffer from rapid or burst release, poor protection at gastric pH, and concerns regarding scalability and safety.[61,62] In contrast, our system exhibited a remarkably controlled, pH-responsive release profile, with only 13% drug release at gastric pH (1.2) over 48 h and 91% cumulative release at intestinal/tumor-mimicking pH (6.8) over the same period. This represents a clear improvement in site-specific release compared to lapatinib alone, which released 56% at gastric pH and only 54% at pH 6.8 within 6 h, thus failing to prevent premature drug loss and providing a limited sustained effect.[63,64] Additionally, this exceeds the gastric protection reported for lapatinib in polymer micelles (30% release at low pH)[65] and represents a substantial improvement over previous MOF carriers lacking biopolymer encapsulation.[66] The higher control and selectivity in the pH-triggered release can be attributed to both the strong MOF-drug interaction and the hydrophilic nature of the SA/PVP matrix, which supports prolonged diffusion and swelling-controlled kinetics.[67]

Tables 6 and 7 represent the *in vitro* drug release kinetics of SA/PVP/Lap-Zr-MOF and lapatinib at 6.8 pH and 1.2 pH, respectively. The values obtained for r^2, K, and n were derived from the mathematical eqn (6)–(9) by linear fitting of the cumulative drug release data. By observing the higher r^2 value obtained by linear fitting of the equations, it is evident that lapatinib drug release follows the Higuchi model at pH 6.8 and the Peppas model at pH 1.2. The SA/PVP/Lap-Zr-MOF system obeyed the Peppas model at both pH values, 6.8 and 1.2. The SA/PVP/Lap-Zr-MOF system obeyed the Peppas model at pH 6.8, indicating that drug release from this system is governed by both the diffusion of the drug and polymer matrix relaxation or swelling. Since the Peppas model describes anomalous transport, this suggests that at a pH near 6.8, the drug release from the system is sustained and controlled, due to the effective and creative interaction between the MOF matrix and the drug.

The value of 'n' indicates the transport mechanism for the investigated systems. The slope value (K) is the same as that of 'n' in the Peppas model. As shown in Tables 6 and 7, at pH 6.8, the 'n' value was less than 0.5 for lapatinib and equal to 0.5 for SA/PVP/Lap-Zr-MOF. This indicates that unsupported lapatinib release follows Fickian diffusion, primarily diffusion-controlled release, and occurs quickly and finishes within a few hours. In the case of SA/PVP/Lap-Zr-MOF, anomalous transport was observed, with a combination of diffusion and polymer swelling or relaxation, which is a more controlled and sustained release compared to the drug alone.[68] At pH 1.2, the 'n' values were close to 1 and 0.93 for lapatinib and SA/PVP/Lap-Zr-MOF, respectively. This indicates case-II transport for both the drug and the system in a constantly controlled manner. SA/PVP/Lap-Zr-MOF has a high degree of control of the drug within the acidic environment, which is useful for preventing premature drug release in the stomach.

Most previous studies on MOF-based or composite carriers demonstrated either a purely diffusion-controlled release (Higuchi model) or a burst followed by a plateau due to less effective matrix-drug or matrix-MOF integration.[69,70] The drug release kinetics best fit the Peppas model at both relevant pH values, indicating

Table 6 *In vitro* drug release kinetics at pH 68

pH 6.8								
	Zero Order		First Order		Higuchi		Korsmeyer–Peppas	
Sample Code	r^2	K	r^2	K	r^2	K	r^2	K
Lap	0.9426	5.2455	0.9879	0.9066	0.9825	0.0019	0.9824	0.3172
SA/PVP/Lap-Zr-MOF	0.7805	1.6614	0.7428	0.2488	0.9342	0.0016	0.9618	0.5375

Table 7 *In vitro* drug release kinetics at pH 12

pH 1.2								
	Zero Order		First Order		Higuchi		Korsmeyer–Peppas	
Sample code	r^2	K	r^2	K	r^2	K	r^2	K
Lap	0.8597	4.8622	0.1910	-0.127	0.9435	0.0019	0.9707	0.2884
SA/PVP/Lap-Zr-MOF	0.7267	0.2185	0.5361	0.0151	0.9155	0.9061	0.9345	0.4821

anomalous (diffusion and relaxation/swelling-driven) transport. Thus, our optimized matrix integration minimized burst release and extended the duration of release, filling a notable gap.

Conclusions

In this study, Zr-MOF (UiO-66) was initially synthesized using a solvothermal method and subsequently combined with an anticancer drug, lapatinib, utilizing its pores. Sodium alginate/polyvinylpyrrolidone (SA/PVP) films in different ratios were prepared using a solvent-casting method and characterized to identify the most effective SA/PVP film formulation. Various weight percentages of lapatinib-loaded Zr-MOF were later integrated with the optimized SA/PVP polymer matrix to develop SA/PVP/lapatinib-loaded Zr-MOF systems. A comprehensive analysis of the mechanical properties of the systems was performed to determine their optimal formulation. A thorough characterization of the synthesized samples was conducted utilizing XRD, FTIR, TGA, and SEM. This analysis confirmed the successful integration of the Zr-MOF and lapatinib systems into the polymer matrix. Investigations into surface wettability, moisture absorption, and swelling ratios further established the physicochemical attributes of the developed systems.

In vitro assessments demonstrated high cell viability, indicating that the prepared films were safe and compatible with biological systems. Additionally, studies on pH-responsive drug release and kinetics revealed a controlled and sustained release profile, particularly under conditions simulating the tumor microenvironment (acidic pH), thereby positioning the system as an optimal candidate for targeted drug delivery. The *in vitro* characteristics, such as sustained and site-specific drug release, suggest that even lower dosages can be effective and side effects can be minimized. This innovative system offers significant promise as an efficient platform for anticancer drug delivery.

Although the *in vitro* results are encouraging, comprehensive *in vivo* investigations are necessary to fully elucidate the pharmacokinetics, biodistribution, long-term safety, and potential immunogenicity of the novel composite system. We currently focus on deepening the mechanistic understanding of cellular uptake and permeability, evaluating efficacy against multidrug-resistant cancer models, and optimizing scalable and reproducible fabrication processes. Additionally, formulation refinements, such as surface modifications and co-delivery of synergistic therapeutics, are being explored to further enhance tumor specificity and therapeutic outcomes. These efforts will advance the translational potential of the new delivery platform, bridging the gap between bench and bedside treatment of HER2-positive cancer.

Author contributions

Sneha Rajeev: conceptualization, methodology, data curation, and writing- original draft preparation. Naja Hasoon KT: writing-review, and editing. Unnikrishnan Gopalakrishna Panicker: Supervision, writing- review, and editing. All authors have discussed, revised, and approved the final version of the manuscript.

Conflicts of interest

There are no conflicts to declare.

Data availability

All data supporting the findings of this study are available within the article. No new data were created or analyzed in this study.

Acknowledgements

Thanks to Biogenix Research Centre for providing the facilities required for *in vitro* cytotoxicity analysis. We thank the Biomedical Technology Wing of the Sree Chitra Tirunal Institute for Medical Sciences and Technology, Trivandrum, for providing the *in vitro* hemocompatibility test requirements. Thanks to the FIST-funded (FIST-No. SR/FST/ET-I/2021/840) SEM Center at the Department of Material Science and Engineering at NIT Calicut for the SEM characterization, and the Central XRD facility at NIT Calicut for providing the XRD characterization.

References

1 R. Kaur, A. Bhardwaj and S. Gupta, *Mol. Biol. Rep.*, 2023, **50**, 9663–9676.
2 I. Salahshoori, M. Golriz, M. A. Nobre, S. Mahdavi, R. E. Malekshah, A. Javdani-Mallak and F. Kargaran, *J. Mol. Liq.*, 2024, **395**, 123888.
3 K. Elumalai, S. Srinivasan and A. Shanmugam, *Biomed. Technol.*, 2024, **5**, 109–122.
4 T. C. Ezike, U. S. Okpala, U. L. Onoja, C. P. Nwike, E. C. Ezeako, O. J. Okpara and B. C. Nwanguma, *Heliyon*, 2023, **9**, e16883.
5 J. Lou, H. Duan, Q. Qin, Z. Teng, F. Gan, X. Zhou and X. Zhou, *Pharmaceutics*, 2023, **15**, 484.
6 S. Gupta, R. Kaur, A. Bhardwaj and D. Parashar, *Indian J. Microbiol.*, 2024, **64**, 1–18.
7 J. Singh and P. Nayak, *J. Polym. Sci.*, 2023, **61**, 2828–2850.

8 Y. Sun and E. Davis, *Nanomaterials*, 2021, **11**, 746.
9 X. Jing, H. Hu, Y. Sun, B. Yu, H. Cong and Y. Shen, *Small Methods*, 2022, **6**, 2101437.
10 T. M. Pham, D. V. Cao, H. H. Q. Dang, P. M. T. Mai, T. B. Nguyen, N. B. N. Dinh and V. T. Le, *J. Mater. Chem. B*, 2024, **12**, 678–690.
11 Q. Yu, L. Ma, L. M. Norona, P. S. Dragovich, J. Wang and S. Wang, *et al.*, *J. Med. Chem.*, 2025, **68**, 16427–16445.
12 X. Wu, H. Sheng, L. Zhao, M. Jiang, H. Lou and Y. Miao, *et al.*, *Cell Death Dis.*, 2022, **13**, 557.
13 A. Spada, J. Emami, J. A. Tuszynski and A. Lavasanifar, *Mol. Pharm.*, 2021, **18**, 1862–1894.
14 E. Hesemans, K. Buttiens, B. B. Manshian and S. J. Soenen, *J. Funct. Biomater.*, 2022, **13**, 137.
15 S. S. Mohammed Ameen and K. M. Omer, *ACS Appl. Mater. Interfaces*, 2024, **16**, 31895–31921.
16 S. Rajeev and U. G. Panicker, *J. Inorg. Organomet. Polym. Mater.*, 2025, **35**, 5157–5188.
17 D. K. Gupta, S. Kumar and M. Y. Wani, *J. Mater. Chem. B*, 2024, **12**, 2691–2710.
18 M. Ishfaq, D. Lateef, Z. Ashraf, M. Sajjad, M. Owais, W. Shoukat, M. Mohsin, M. Ibrahim, F. Verpoort and A. H. Chughtai, *RSC Adv.*, 2025, **15**, 26647–26659.
19 T. Wen, G. Quan, B. Niu, Y. Zhou, Y. Zhao, C. Lu, X. Pan and C. Wu, *Small*, 2021, **17**, 2005064.
20 H. Nabipour, F. Aliakbari, K. Volkening, M. J. Strong and S. Rohani, *Int. J. Biol. Macromol.*, 2024, **259**, 128875.
21 M. A. Abourehab, R. R. Rajendran, A. Singh, S. Pramanik, P. Shrivastav, M. J. Ansari and A. Deepak, *Int. J. Mol. Sci.*, 2022, **23**, 9035.
22 B. Foroughi-Nia, J. Barar, M. Y. Memar, A. Aghanejad and S. Davaran, *Life Sci.*, 2021, **278**, 119642.
23 S. Eljack, S. David, I. Chourpa, A. Faggad and E. Allard-Vannier, *Pharmaceuticals*, 2022, **15**, 1452.
24 E. Aslan, *Development and Investigation of the Efficacy of Lapatinib Loaded Targeted Drug Delivery Nanosystem for Breast Cancer Treatment*, MS thesis, Izmir Institute of Technology, Izmir, 2024.
25 M. Keerikkadu, P. D. Bangera, V. K. Tippavajhala and M. Rathnanand, *AAPS PharmSciTech*, 2025, **26**, 131.
26 Y. Wang and C. Wang, *Pharmaceutics*, 2022, **14**, 1150.
27 N. S. Değirmenci, M. Uslu, O. K. Kırbaş, F. Şahin and E. Ö. Uçar, *J. Drug Delivery Sci. Technol.*, 2022, **75**, 103584.
28 N. B. Fernandes, V. Velagacherla, K. J. Spandana, C. H. Mehta, S. Gadag, J. N. Sabhahit and U. Y. Nayak, *Int. J. Pharm.*, 2024, **650**, 123686.
29 X. Su, T. Xu, R. Ye, C. Guo, S. M. Wabaidur, D. L. Chen and Y. Hu, *J. Colloid Interface Sci.*, 2023, **646**, 129–140.
30 A. K. El-Sawaf, A. M. Abdelgawad, A. A. Nassar and D. A. Elsherbiny, *Int. J. Biol. Macromol.*, 2024, **274**, 133438.
31 B. Hassanpour and V. M. Karbhari, *Polymers*, 2024, **16**, 2265.
32 F. Bonafè, C. Dong, G. G. Malliaras, T. Cramer and B. Fraboni, *ACS Appl. Mater. Interfaces*, 2024, **16**, 36727–36734.
33 L. Li, L. Mao and J. Yang, *Adv. Mater. Technol.*, 2025, **10**, 2401175.
34 B. K. Wilson and R. K. Prud'homme, *J. Colloid Interface Sci.*, 2021, **604**, 208–220.
35 Y. Khan, H. Sadia, S. Z. Ali Shah, M. N. Khan, A. A. Shah, N. Ullah and M. I. Khan, *Catalysts*, 2022, **12**, 1386.
36 A. K. Atef, T. B. Mostafa and H. M. El-Sherif, *Sci. Rep.*, 2025, **15**, 10224.
37 R. Fang, N. Yu, F. Wang, X. Xu and J. Zhang, *ACS Appl. Mater. Interfaces*, 2025, **17**, 9087–9102.
38 P. K. Pandey, P. P. Singh, S. Khatua, R. Ranganathan and A. Mishra, *ACS Appl. Mater. Interfaces*, 2024, **17**, 663–674.
39 M. M. Mathew, M. Gopika and G. Unnikrishnan, *Int. J. Biol. Macromol.*, 2024, **277**, 134183.
40 J. Zhang, Y. Zhou, J. Guo, M. Yan, C. Liu and B. Du, *ACS Appl. Mater. Interfaces*, 2025, **17**, 6689–6702.
41 M. Aslam, B. Fatima, R. Batool, M. Imran, D. Hussain, M. Najam-ul-Haq and R. Mehmood, *ACS Appl. Mater. Interfaces*, 2025, **17**, 26263–26281.
42 M. Askarizadeh, N. Esfandiari, B. Honarvar, S. A. Sajadian and A. Azdarpour, *ChemBioEng Rev.*, 2023, **10**, 1006–1049.
43 M. Kandiah, S. Usseglio, S. Svelle, U. Olsbye, K. P. Lillerud and M. Tilset, *J. Mater. Chem.*, 2010, **20**, 9848–9851.
44 M. A. Alam, S. Ahmed, R. K. Bishwas, S. Mostofa, S. A. Jahan and S. Afr, *J. Chem. Eng.*, 2025, **51**, 68–77.
45 P. Varlashkin, *Powder Diffr.*, 2009, **24**, 250–253.
46 K. Chakarova, I. Strauss, M. Mihaylov, N. Drenchev and K. Hadjiivanov, *Microporous Mesoporous Mater.*, 2019, **281**, 110–122.
47 A. A. Mohammadi, A. Alinejad, B. Kamarehie, S. Javan, A. Ghaderpoury, M. Ahmadpour and M. Ghaderpoori, *Int. J. Environ. Sci. Technol.*, 2017, **14**, 1959–1968.
48 N. Gumber, R. V. Pai, K. Sanyal, B. Dutta and P. A. Hassan, *Microporous Mesoporous Mater.*, 2022, **341**, 112108.
49 M. A. El-Bindary, M. G. El-Desouky and A. A. El-Bindary, *Appl. Organomet. Chem.*, 2022, **36**, e6660.
50 Y. Shi, Y. Zhang, L. Zhu, Y. Miao, Y. Zhu and B. Yue, *Adv. Healthcare Mater.*, 2024, **13**, 2301726.
51 A. M. Abdelghany, A. H. Oraby and M. O. Farea, *Phys. B*, 2019, **560**, 162–173.
52 S. Kalyani, B. Smitha, S. Sridhar and A. Krishnaiah, *Ind. Eng. Chem. Res.*, 2006, **45**, 9088–9095.
53 M. C. Pires, D. Sousa and M. F. C. G. Silva, *Pharmaceutics*, 2020, **12**, 865.
54 L. K. Vora, H. McMillian, D. Mishra, D. Jones and R. R. S. Thakur, *J. Pharm. Sci.*, 2025, **114**, 103717.
55 M. A. Beach, U. Nayanathara, Y. Gao, C. Zhang, Y. Xiong, Y. Wang and G. K. Such, *Chem. Rev.*, 2024, **124**, 5505–5616.
56 S. Adepu and S. Ramakrishna, *Molecules*, 2021, **26**, 5905.
57 S. Li, S. M. Yan, L. W. Zhang, X. Y. Yang and Z. Guo, *Front. Pharmacol.*, 2025, **16**, 1530650.
58 S. Malehmir, M. A. Esmaili, M. Khaksary Mahabady, A. Sobhani-Nasab, A. Atapour, M. R. Ganjali and A. Moradi Hasan-Abad, *Front. Chem.*, 2023, **11**, 1249134.
59 L. Khalef, R. Lydia, K. Filicia and B. Moussa, *Cell Biochem. Funct.*, 2024, **42**, e4007.
60 A. Foti, L. Calì, S. Petralia and C. Satriano, *Nanomaterials*, 2023, **13**, 1624.
61 S. S. Saremi, A. R. Nikpoor, K. Sadri, A. Mehrabian, M. Karimi, A. Mansouri and A. Badiee, *Colloids Surf., B*, 2021, **207**, 112012.

62 N. Singh, R. Chakravarti, A. Das, S. Gupta, D. Ghosh and P. Datta, *Mol. Pharm.*, 2024, **21**, 3921–3935.
63 S. Dewangan, N. Singh, O. K. Gaikwad, R. Chakravarti, P. Das, D. Ghosh and P. Datta, *Mol. Pharm.*, 2025, **22**, 5037–5049.
64 X. Liu, Y. Chen and J. Huang, *Mol. Pharm.*, 2020, **17**, 3982–3992.
65 H. Lu, T. Chen, Y. Wang, Y. He, Z. Pang and Y. Wang, *Sci. Rep.*, 2022, **12**, 2610.
66 X. Wu, H. Sheng, L. Zhao, M. Jiang, H. Lou, Y. Miao and W. Li, *Cell Death Dis.*, 2022, **13**, 557.
67 Z. Gong, H. Zhao and J. Bai, *Colloids Surf., B*, 2024, **239**, 113954.
68 D. G. Dastidar, A. Biswas, A. Das, S. Naskar and R. Mahish, *Drug Metab. Bioanal. Lett.*, 2024, **17**, 121–136.
69 P. Verma, M. S. Bannon, M. K. Kuenen, S. Raj, A. Dhakal, K. Stone and G. Giri, *Chem. Mater.*, 2024, **36**, 9356–9369.
70 A. Anim, L. A. Mahmoud, A. L. Kelly, M. G. Katsikogianni and S. Nayak, *Appl. Sci.*, 2023, **13**, 10611.